arXiv:2004.10095v2 [astro-ph.EP] 8 May 2020

The multi-planet system TOI-421
A warm Neptune and a super puffy mini-Neptune transiting a G9 V star in a visual binary[*]

Ilaria Carleo,[1,2] Davide Gandolfi,[3] Oscar Barragán,[4] John H. Livingston,[5] Carina M. Persson,[6] Kristine W. F. Lam,[7] Aline Vidotto,[8] Michael B. Lund,[9] Carolina Villarreal DAngelo,[8] Karen A. Collins,[10] Luca Fossati,[11] Andrew W. Howard,[12] Daria Kubyshkina,[11,8] Rafael Brahm,[13,14] Antonija Oklopčić,[10,15] Paul Mollière,[16] Seth Redfield,[1] Luisa Maria Serrano,[3,17,18] Fei Dai,[19,20] Malcolm Fridlund,[6,21] Francesco Borsa,[22] Judith Korth,[23] Massimiliano Esposito,[24] Matías R. Díaz,[25] Louise Dyregaard Nielsen,[26] Coel Hellier,[27] Savita Mathur,[28,29] Hans J. Deeg,[28,29] Artie P. Hatzes,[24] Serena Benatti,[30] Florian Rodler,[31] Javier Alarcon,[31] Lorenzo Spina,[32,33] Ângela R. G. Santos,[34] Iskra Georgieva,[6] Rafael A. García,[35,36] Lucía González-Cuesta,[28] George R. Ricker,[37] Roland Vanderspek,[37] David W. Latham,[10] Sara Seager,[37,38,39] Joshua N. Winn,[40] Jon M. Jenkins,[41] Simon Albrecht,[42] Natalie M. Batalha,[43] Corey Beard,[44] Patricia T. Boyd,[45] François Bouchy,[46] Jennifer A. Burt,[47] R. Paul Butler,[48] Juan Cabrera,[49] Ashley Chontos,[50,†] David Ciardi,[9] William D. Cochran,[51] Kevin I. Collins,[52] Jeffrey D. Crane,[53] Ian Crossfield,[54] Szilard Csizmadia,[49] Diana Dragomir,[55] Courtney Dressing,[56] Philipp Eigmüller,[49] Michael Endl,[51] Anders Erikson,[49] Nestor Espinoza,[57] Michael Fausnaugh,[37] Fabo Feng,[48] Erin Flowers,[40] Benjamin Fulton,[9] Erica J. Gonzales,[58] Nolan Grieves,[46] Sascha Grziwa,[23] Eike W. Guenther,[24] Natalia M. Guerrero,[37] Thomas Henning,[59] Diego Hidalgo,[28] Teruyuki Hirano,[60] Maria Hjorth,[42] Daniel Huber,[50] Howard Isaacson,[61,62] Matias Jones,[31] Andrés Jordán,[13,14] Petr Kabáth,[63] Stephen R. Kane,[64] Emil Knudstrup,[42] Jack Lubin,[44] Rafael Luque,[28,29] Ismael Mireles,[37] Norio Narita,[5,28,65,66,67] David Nespral,[28,29] Prajwal Niraula,[68] Grzegorz Nowak,[28,29] Enric Palle,[28,29] Martin Pätzold,[23] Erik A Petigura,[69] Jorge Prieto-Arranz,[28,29] Heike Rauer,[7,49,70] Paul Robertson,[44] Mark E. Rose,[41] Arpita Roy,[12] Paula Sarkis,[71] Joshua E. Schlieder,[45] Damien Ségransan,[46] Stephen Shectman,[53] Marek Skarka,[63,72] Alexis M. S. Smith,[49] Jeffrey C. Smith,[73] Keivan Stassun,[74] Johanna Teske,[53,75] Joseph D. Twicken,[73] Vincent Van Eylen,[76] Sharon Wang,[53] Lauren M. Weiss,[50] and Aurélien Wyttenbach[46,77,78]

[1]Astronomy Department and Van Vleck Observatory, Wesleyan University, Middletown, CT 06459, USA
[2]INAF – Osservatorio Astronomico di Padova, Vicolo dell'Osservatorio 5, I-35122, Padova, Italy
[3]Dipartimento di Fisica, Università degli Studi di Torino, via Pietro Giuria 1, I-10125, Torino, Italy
[4]Sub-department of Astrophysics, Department of Physics, University of Oxford, Oxford, OX1 3RH, UK
[5]Department of Astronomy, University of Tokyo, 7-3-1 Hongo, Bunkyo-ku, Tokyo 113-0033, Japan
[6]Department of Space, Earth and Environment, Chalmers University of Technology, Onsala Space Observatory, 439 92 Onsala, Sweden
[7]Center for Astronomy and Astrophysics, TU Berlin, Hardenbergstr. 36, 10623 Berlin, Germany
[8]School of Physics, Trinity College Dublin, The University of Dublin College Green, Dublin 2, Dublin, Ireland
[9]NASA Exoplanet Science Institute/Caltech-IPAC, MC 314-6, 1200 E California Blvd, Pasadena, CA 91125, USA
[10]Center for Astrophysics | Harvard & Smithsonian, 60 Garden Street, Cambridge, MA 02138, USA
[11]Space Research Institute, Austrian Academy of Sciences, Schmiedlstrasse 6, A-8041 Graz, Austria
[12]Department of Astronomy, California Institute of Technology, Pasadena, CA 91125, USA
[13]Facultad de Ingeniería y Ciencias, Universidad Adolfo Ibáñez, Av.Diagonal las Torres 2640, Peñalolén, Santiago, Chile
[14]Millennium Institute for Astrophysics, Chile
[15]NHFP Sagan Fellow
[16]Max-Planck-Institut für Astronomie, Königstuhl 17, 69117 Heidelberg, Germany
[17]Instituto de Astrofísica e Ciências do Espaço, Universidade do Porto, CAUP, Rua das Estrelas, PT4150-762 Porto, Portugal
[18]Departamento de Física e Astronomia, Faculdade de Ciências, Universidade do Porto, Rua Campo Alegre, 4169-007 Porto, Portugal
[19]Department of Physics and Kavli Institute for Astrophysics and Space Research, MIT, Cambridge, MA 02139, USA
[20]Department of Astrophysical Sciences, Princeton University, 4 Ivy Lane, Princeton, NJ, 08544, USA
[21]Leiden Observatory, University of Leiden, PO Box 9513, 2300 RA, Leiden, The Netherlands
[22]INAF - Osservatorio Astronomico di Brera, Via E. Bianchi 46, 23807 Merate, Italy
[23]Rheinisches Institut für Umweltforschung an der Universität zu Köln, Aachener Strasse 209, 50931 Köln, Germany
[24]Thüringer Landessternwarte Tautenburg, Sternwarte 5, D-07778 Tautenburg, Germany
[25]Departamento de Astronomía, Universidad de Chile, Camino El Observatorio 1515, Las Condes, Santiago, Chile
[26]Geneva Observatory, University of Geneva, Chemin des Maillettes 51, CH1290 Versoix, Switzerland

Corresponding author: Ilaria Carleo
icarleo@wesleyan.edu

^{27}*Astrophysics Group, Keele University, Staffordshire, ST5 5BG, UK*

^{28}*Instituto de Astrofísica de Canarias, C/Vía Láctea s/n, 38205 La Laguna, Spain*

^{29}*Departamento de Astrofísica, Universidad de La Laguna, 38206 La Laguna, Spain*

^{30}*INAF - Osservatorio Astronomico di Palermo, Piazza del Parlamento, 1, I-90134 Palermo, Italy*

^{31}*European Southern Observatory (ESO), Alonso de Córdova 3107, Vitacura, Casilla 19001, Santiago de Chile*

^{32}*School of Physics and Astronomy, Monash University, VIC 3800, Australia*

^{33}*ARC Centre of Excellence for All Sky Astrophysics in Three Dimensions (ASTRO-3D)*

^{34}*Space Science Institute, 4765 Walnut Street, Suite B, Boulder CO 80301, USA*

^{35}*IRFU, CEA, Université Paris-Saclay, Gif-sur-Yvette, France*

^{36}*AIM, CEA, CNRS, Université Paris-Saclay, Université Paris Diderot, Sorbonne Paris Cité, F-91191 Gif-sur-Yvette, France*

^{37}*Department of Physics and Kavli Institute for Astrophysics and Space Research, Massachusetts Institute of Technology, Cambridge, MA 02139, USA*

^{38}*Department of Earth, Atmospheric and Planetary Sciences, Massachusetts Institute of Technology, Cambridge, MA 02139, USA*

^{39}*Department of Aeronautics and Astronautics, MIT, 77 Massachusetts Avenue, Cambridge, MA 02139, USA*

^{40}*Department of Astrophysical Sciences, Princeton University, 4 Ivy Lane, Princeton, NJ 08544, USA*

^{41}*NASA Ames Research Center, Moffett Field, CA, 94035, USA*

^{42}*Stellar Astrophysics Centre, Dep. of Physics and Astronomy, Aarhus University, Ny Munkegade 120, DK-8000 Aarhus C, Denmark*

^{43}*Department of Astronomy and Astrophysics, University of California, Santa Cruz, CA 95060, USA*

^{44}*Department of Physics & Astronomy, University of California Irvine, Irvine, CA 92697, USA*

^{45}*NASA Goddard Space Flight Center, Greenbelt, MD*

^{46}*Geneva Observatory, University of Geneva, Chemin des Mailettes 51, 1290 Versoix, Switzerland*

^{47}*Jet Propulsion Laboratory, California Institute of Technology, 4800 Oak Grove drive, Pasadena CA 91109, USA*

^{48}*Carnegie Institution for Science, Earth & Planets Laboratory, 5241 Broad Branch Road NW, Washington DC 20015, USA*

^{49}*Institute of Planetary Research, German Aerospace Center, Rutherfordstrasse 2, 12489 Berlin, Germany*

^{50}*Institute for Astronomy, University of Hawai'i, 2680 Woodlawn Drive, Honolulu, HI 96822, USA*

^{51}*Department of Astronomy and McDonald Observatory, University of Texas at Austin, 2515 Speedway, Stop C1400, Austin, TX 78712, USA*

^{52}*George Mason University, 4400 University Drive, Fairfax, VA, 22030 USA*

^{53}*Observatories of the Carnegie Institution for Science, 813 Santa Barbara Street, Pasadena, CA 91101*

^{54}*Department of Physics & Astronomy, University of Kansas, 1082 Malott,1251 Wescoe Hall Dr., Lawrence, KS 66045, USA*

^{55}*Department of Physics and Astronomy, University of New Mexico,Albuquerque, NM, USA*

^{56}*501 Campbell Hall, University of California at Berkeley, Berkeley, CA 94720, USA*

^{57}*Space Telescope Science Institute, 3700 San Martin Drive, Baltimore, MD 21218, USA*

^{58}*Department of Astronomy and Astrophysics, University of California, Santa Cruz, 1156 High St. Santa Cruz , CA 95064, USA*‡

^{59}*Max-Planck-Institut für Astronomie, Königstuhl 17, Heidelberg69117, Germany*

^{60}*Department of Earth and Planetary Sciences, Tokyo Institute of Technology, 2-12-1 Ookayama, Meguro-ku, Tokyo 152-8551, Japan*

^{61}*Department of Astronomy, University of California Berkeley, Berkeley CA 94720*

^{62}*Centre for Astrophysics, University of Southern Queensland, Toowoomba, QLD, Australia*

^{63}*Astronomical Institute, Czech Academy of Sciences, Fričova 298, 25165, Ondřejov, Czech Republic*

^{64}*Department of Earth and Planetary Sciences, University of California, Riverside, CA 92521, USA*

^{65}*Astrobiology Center, NINS, 2-21-1 Osawa, Mitaka, Tokyo 181-8588, Japan*

^{66}*National Astronomical Observatory of Japan, NINS, 2-21-1 Osawa, Mitaka, Tokyo 181-8588, Japan*

^{67}*JST, PRESTO, 7-3-1 Hongo, Bunkyo-ku, Tokyo 113-0033, Japan*

^{68}*Department of Earth, Atmospheric and Planetary Sciences, Massachusetts Institute of Technology, Cambridge, MA 02139*

^{69}*Department of Physics & Astronomy, University of California Los Angeles, Los Angeles, CA 90095, USA*

^{70}*Institute of Geological Sciences, FU Berlin, Malteserstr. 74-100, D-12249 Berlin*

^{71}*Max-Planck-Institut für Astronomie, Königstuhl 17, Heidelberg, 69117, Germany*

^{72}*Department of Theoretical Physics and Astrophysics, Masaryk University, Kotlářská 2, 61137 Brno, Czech Republic*

^{73}*SETI Institute/NASA Ames Research Center, Moffett Field, CA, 94035, USA*

^{74}*Department of Physics & Astronomy, Vanderbilt University, Nashville, TN, USA*

^{75}*NASA Hubble Fellow*

^{76}*Mullard Space Science Laboratory, University College London, Holmbury St Mary, Dorking, Surrey, RH5 6NT, UK*

^{77}*Leiden Observatory, P.O. Box 9513, NL-2300 RA Leiden, The Netherlands*

^{78}*Universit Grenoble Alpes, CNRS, IPAG, 38000 Grenoble, France*

ABSTRACT

We report the discovery of a warm Neptune and a hot sub-Neptune transiting TOI-421 (BD-14 1137, TIC 94986319), a bright (V=9.9) G9 dwarf star in a visual binary system observed by the *TESS* space mission in Sectors 5 and 6. We performed ground-based follow-up observations – comprised of LCOGT transit photometry, NIRC2 adaptive optics imaging, and FIES, CORALIE, HARPS, HIRES, and PFS high-precision Doppler measurements – and confirmed the planetary nature of the 16-day transiting candidate announced by the *TESS* team. We discovered an additional radial velocity signal with a period of 5 days induced by the presence of a second planet in the system, which we also found to transit its host star. We found that the outer warm Neptune, TOI-421 b, has an orbital period of $P_b = 16.06815^{+0.00034}_{-0.00035}$ days, a mass of $M_b = 16.23^{+1.14}_{-1.08}$ $M_\oplus$, a radius of $R_b = 5.17^{+0.13}_{-0.13}$ $R_\oplus$ and a density of $\rho_b = 0.645^{+0.069}_{-0.062}$ g cm^{-3}, whereas the inner mini-Neptune, TOI-421 c, has a period of $P_c = 5.19676^{+0.00049}_{-0.00048}$ days, a mass of $M_c = 7.05^{+0.71}_{-0.70}$ $M_\oplus$ and a radius of $R_c = 2.72^{+0.19}_{-0.18}$ $R_\oplus$. With its characteristics the latter planet ($\rho_c = 1.93^{+0.49}_{-0.39}$ g cm^{-3}) is placed in the intriguing class of the super-puffy mini-Neptunes. TOI-421 b and c are found to be well suitable for atmospheric characterization. Our atmospheric simulations predict significant Ly-α transit absorption, due to strong hydrogen escape in both planets, and the presence of detectable CH$_4$ in the atmosphere of TOI-421 b if equilibrium chemistry is assumed.

Keywords: Exoplanet astronomy: Exoplanet systems — High resolution spectroscopy — stars: fundamental parameters — techniques: radial velocities, spectroscopic, photometric

1. INTRODUCTION

The *TESS* (*Transiting Exoplanet Survey Satellite*, Ricker et al. 2014) mission's primary scientific driver is to measure masses for transiting planets smaller than 4 $R_\oplus$ around bright stars, in order to explore the transition from sub-Neptunes (with extended envelopes) to rocky planets (with compact atmospheres), that occurs at about 1.8 $R_\oplus$. The *Kepler* mission revealed that small planets (especially in the super-Earth and sub-Neptune regime), in compact coplanar multi-planet systems, are very common (Latham et al. 2011; Lissauer et al. 2011, 2014; Rowe et al. 2014). While most of *Kepler* stars are distant and faint, making radial velocity (RV) follow-up very difficult, the *TESS* mission is focused on the nearest and brightest stars, so that an intensive follow-up, as well as atmospheric characterization, can more easily be achieved. Those prospects are rather important, for example for future space-based observations with *JWST*.

Since July 2018 *TESS* has been scanning the sky and performing a photometric search for planets transiting bright stars. In its primary mission, this survey will cover 26 Sectors, each of them monitored for ~27 days, with candidate alerts released almost every month. *TESS* is expected to detect ~10,000 transiting exoplanets (Sullivan et al. 2015; Barclay et al. 2018; Huang et al. 2018a). More than 1,000 planet candidates have been revealed, with dozens of confirmed planets so far (e.g. Esposito et al. 2019; Brahm et al. 2019a; Lendl et al. 2020; Díaz et al. 2020), some of which are multi-planet systems (e.g, Gandolfi et al. 2018; Huang et al.

2018b; Dragomir et al. 2019; Günther et al. 2019; Quinn et al. 2019; Gandolfi et al. 2019).

Multi-planet systems are prime targets for testing planetary formation and evolution theories. Orbiting the same star, they offer an opportunity to simplify the assumptions of initial conditions and compare planets with different sizes and compositions in the same system. Such systems are also interesting for transmission spectroscopy, which allows us to characterize planetary atmospheres and compare them at different levels of incident stellar flux.

In the present paper we report on the discovery and characterization of a Neptune (TOI-421 b) and a sub-Neptune (TOI-421 c) transiting the bright star BD-14 1137 (TOI-421, TIC 94986319), observed by *TESS* in Sectors 5 and 6. The work presented here is part of the RV follow-up project carried out by the KESPRINT collaboration[1] (e.g., Grziwa et al. 2016; Van Eylen et al. 2016; Gandolfi et al. 2017; Nowak et al. 2017; Barragán et al. 2018; Persson et al. 2019; Korth et al. 2019), which aims to confirm and characterize planet candidates from the *K2* and *TESS* space missions.

This paper is organized as follows. In Section 2, we describe the observations carried out with different space- and ground-based facilities. These include *TESS* photometry, AO imaging, ground-based photometry, and high-resolution spectroscopy. In Section 3 we derive the stellar parameters of TOI-421. Section 4 reports the *TESS* photometry analysis with the detection of the transit signals. Section 6 presents the HARPS frequency analysis to confirm the planetary nature of the transiting companions and investigate additional signals associated to the stellar activity. Sections 7 and 8

[†] NSF Graduate Research Fellow

[‡] National Science Foundation Graduate Research Fellow

[1] www.kesprint.science.

Table 1. Main identifiers, equatorial coordinates, proper motion, parallax, optical and infrared magnitudes, and fundamental parameters of TOI-421.

Parameter	Value	Source
Main identifiers		
TIC	94986319	ExoFOP
BD	-14 1137	ExoFOP
TYC	5344-01206-1	ExoFOP
2MASS	J05272482-1416370	ExoFOP
Equatorial coordinates, parallax, and proper motion		
R.A. (J2000.0)	$05^{\rm h}27^{\rm m}24.83^{\rm s}$	*Gaia* DR2
Dec. (J2000.0)	$-14°16'37.05''$	*Gaia* DR2
π (mas)	13.3407 ± 0.0361	*Gaia* DR2
μ_α (mas yr^{-1})	-35.687 ± 0.046	*Gaia* DR2
μ_δ (mas yr^{-1})	50.450 ± 0.064	*Gaia* DR2
Optical and near-infrared photometry		
TESS	9.2711 ± 0.006	TIC v8
G	9.7778 ± 0.0002	*Gaia* DR2
$B_{\rm p}$	10.2034 ± 0.0012	*Gaia* DR2
$R_{\rm p}$	9.2265 ± 0.0012	*Gaia* DR2
B	10.735 ± 0.076	TIC v8
V	9.931 ± 0.006	TIC v8
J	8.547 ± 0.020	2MASS
H	8.219 ± 0.033	2MASS
Ks	8.071 ± 0.018	2MASS
$W1$	8.058 ± 0.023	All*WISE*
$W2$	8.110 ± 0.020	All*WISE*
$W3$	8.060 ± 0.021	All*WISE*
$W4$	7.809 ± 0.168	All*WISE*
Fundamental parameters		
$v \sin i_\star$ (km s^{-1})	1.8 ± 1.0	This work
$T_{\rm eff}$ (K)	5325^{+78}_{-58}	This work
$\log g_\star$ (cgs)	$4.486^{+0.025}_{-0.018}$	This work
[Fe/H] (dex)	-0.02 ± 0.05	This work
$M_\star$ ($M_\odot$)	$0.852^{+0.029}_{-0.021}$	This work
$R_\star$ ($R_\odot$)	0.871 ± 0.012	This work
Age (Gyr)	$9.4^{+2.4}_{-3.1}$	This work
Distance (pc)	74.94 ± 0.58	This work
$A_{\rm V}$ (mag)	$0.11^{+0.12}_{-0.08}$	This work

present a preliminary RV modeling and a joint analysis of *TESS* light curve and RV data, respectively. We discuss the results in Section 9, including the simulations of possible atmospheric signals in different wavelength bands and of the atmospheric evolution of both planets. Finally, we draw our conclusion in Section 10.

2. OBSERVATIONS

2.1. TESS *photometry*

TOI-421 (TIC 94986319) – whose identifiers, coordinates, proper motion, optical and infrared magnitudes, and fundamental parameters are listed in Table 1 – was monitored in Sectors 5 and 6 of the *TESS* mission between 15 November 2018 and 07 January 2019. In Sector 5, the target was imaged on CCD 3 of camera 2, and on CCD 4 of camera 2 in Sector 6. A total of 34,622 photometric data points were collected, each with an exposure time of 2 minutes. The target light curves were processed by the Science Processing Operations Center (SPOC; Jenkins et al. 2016) data reduction pipeline. The Simple Aperture Photometry (SAP) was used in the SPOC pipeline to produce the light curves (Twicken et al. 2010; Morris et al. 2017), and the Presearch Data Conditioning (PDCSAP) algorithm was used to remove known instrumental systematics (Smith et al. 2012; Stumpe et al. 2012, 2014). For the transit detection and analysis presented in this work (Sec. 4), we downloaded TOI-421's PDCSAP light curves, which are publicly available at the Mikulski Archive for Space Telescopes (MAST) web-page[2].

2.2. *Ground-based Photometry*

2.2.1. *LCOGT*

We observed TOI-421 in Pan-STARSS Y-band on UT 2019-02-05 using the South Africa Astronomical Observatory node of the Las Cumbres Observatory Global Telescope (LCOGT) 1-m network (Brown et al. 2013). We used the `TESS Transit Finder`, which is a customized version of the `Tapir` software package (Jensen 2013), to schedule our transit observation. The 1-m telescopes are equipped with 4096×4096 LCO SINISTRO cameras having an image scale of 0.389″ pixel^{-1} resulting in a 26′ × 26′ field of view. The images were calibrated using the standard LCOGT BANZAI pipeline (McCully et al. 2018) and the photometric data were extracted using the `AstroImageJ` (`AIJ`) software package (Collins et al. 2017). The images have a mean stellar PSF FWHM of 1.78″. The optimum target star photometric aperture used to extract the data for the analyses in this work had a radius of 15 pixels (5.8″). Furthermore, the transit was detected in apertures as small as 5 pixels (1.9″) with higher model residuals.

2.2.2. *WASP-South*

The field of TOI-421 was also observed by WASP-South each year from 2008 to 2015, covering a span of ~120 nights per year. WASP-South was an array of 8 cameras located in Sutherland, South Africa, being the Southern station of the WASP project (Pollacco et al. 2006). Until 2012 it used 200-mm, f/1.8 lenses, observing fields with a typical 10-min

---

cadence, and accumulated 14 800 photometric data points on TOI-421. It then switched to 85-mm, f/1.2 lenses using an SDSS-r filter, and accumulated another 77 000 observations of TOI-421. We did not find any significant periodicity.

2.3. *AO Imaging*

High-resolution adaptive optics (AO) imaging observations of TOI-421 were made with NIRC2 on Keck II (http://www2.keck.hawaii.edu/inst/nirc2/) on 2019 Mar 25 UT. Weather was dry and stable but clouds affected the observations throughout the night. Extinction due to clouds was estimated to be between 1.2 - 3 magnitudes. TOI-421 was observed at an airmass of 1.5. Observations were made in natural guide star, narrow camera (0.009942 ″/pixel) mode, and used the full $1024'' \times 1024''$ FOV. A standard 3-point dither pattern was used to avoid the noisy lower left quadrant of the detector. Each pointing was done with a 3″ nod to find any off-axis bright sources. Observations were made in the K-band for a total integration time of 180 seconds once all pointings were co-added. The AO observations of TOI-421 resulted in a spatial resolution of 0.053″ (FWHM) in the K-band.

2.4. *Ground-based Spectroscopy*

We carried out spectroscopic follow-up observations of TOI-421 using different facilities – as described in the subsections below – to spectroscopically confirm the planetary nature of the transit signals detected in the *TESS* light curve and determine the masses of the two transiting planets.

2.4.1. *FIES*

We started the radial velocity follow-up of TOI-421 in February 2019 using the FIbre-fed Echellé Spectrograph (FIES; Frandsen & Lindberg 1999; Telting et al. 2014) mounted at the 2.56 m Nordic Optical Telescope (NOT) of Roque de los Muchachos Observatory (La Palma, Spain). FIES is mounted inside an insulated building where the temperature is kept constant within 0.02 C and fed with octagonal fibres to improve the radial velocity (RV) stability of the spectrograph (Stürmer et al. 2018). We employed the intermediate resolution fibre, which provides a resolving power of R = 45 000 over the wavelength range 3660 - 9275 Å, and acquired 10 spectra between 2 February and 13 March 2019. We used the same observing strategy as in Buchhave et al. (2010) and Gandolfi et al. (2013), i.e., we split the observations in three sub-exposures to remove cosmic ray hits and bracketed the three exposures with long-exposed ($T_{exp} \approx 80$ sec) ThAr spectra to trace the instrument drift and improve the wavelength solution. We reduced the data using IRAF and IDL standard procedures and extracted relative RV measurements by cross-correlating the observed Echellé spectra with the first epoch spectrum (Table 6).

2.4.2. *CORALIE*

We also took 7 high-resolution spectra ($R \approx 60\,000$) of TOI-421 using the CORALIE Echellé spectrograph on the Swiss 1.2 m Euler telescope at La Silla Observatories, Chile (Queloz et al. 2001). We extracted the radial velocity measurements by cross-correlating the CORALIE Echellé spectra with a binary G2 mask (Pepe et al. 2002). The Doppler measurements show no significant RV variation at a level of ~8 m s^{-1} and exclude that TOI-421 is an eclipsing binary mimicking planetary transits.

2.4.3. *HARPS*

We acquired 105 high-resolution ($R = 115\,000$) spectra of TOI-421 using the High Accuracy Radial velocity Planet Searcher (HARPS Mayor et al. 2003) spectrograph mounted at the ESO-3.6 m telescope of La Silla Observatory, Chile. Installed in a pressure- and temperature-controlled enclosure and fed with octagonal fibres, HARPS has demonstrated a long-term precision at the 1 m s^{-1} level and below (Lovis et al. 2006). Our HARPS observations were performed over two observing seasons between February 2019 and January 2020, as part of the observing programs 1102.C-0923, 0103.C-0874, 0103.C-0759, 0103.C-0442, and 60.A-9709. We used the second fibre of the instrument to monitor the sky background and set the exposure time to 900-2100 sec depending on sky conditions and constraints of the observing schedule. We reduced the data using the dedicated HARPS Data Reduction Software (DRS) and computed the RVs by cross-correlating the Échelle spectra with a G2 numerical mask (Baranne et al. 1996; Pepe et al. 2002; Lovis & Pepe 2007). We also used the DRS to extract the line profile asymmetry indicators, namely, the full width at half maximum (FWHM) and the bisector inverse slope (BIS) of the cross-correlation function (CCF), and the Ca ɪɪ H & K lines activity indicator[3] log R′$_{HK}$. We report the HARPS RV measurements and their uncertainties, along with the FWHM, BIS, log R′$_{HK}$, exposure time, and signal-to-noise (S/N) ratio per pixel at 550 nm in Table 4.

2.4.4. *HIRES*

Between 17 September 2019 and 3 March 2020, we obtained 28 spectra ($R = 55\,000$) of TOI-421 over 27 nights using the High Resolution Échelle Spectrometer (HIRES; Vogt et al. 1994) on the 10-m Keck-I telescope. The spectra were collected using an iodine cell for wavelength reference. The median exposure time was 680 s, which allowed us to achieve a S/N ratio of 200 per reduced pixel at 5500 Å. We also obtained a high S/N ratio template spectrum without the iodine cell, which was used as input for the standard

---

[3] We adopted a B−V color index of 0.710, as listed in the APASS catalog (Henden et al. 2015).

forward-modeling procedures of the California Planet Search
(Howard et al. 2010). We report the RVs and uncertainties
based on the weighted mean and weighted error in the mean
of the ~700 individual spectral chunks in Table 5.

2.4.5. *PFS*

TOI-421 was also selected as a high priority target by the
WINE (Warm gIaNts with tEss) collaboration, which aims
at systematically characterizing long period transiting giant
and Neptune-size planets from the *TESS* mission (see, e.g.,
Brahm et al. 2019b; Jordán et al. 2019). In this context,
we monitored TOI-421 with the Planet Finder Spectrograph
(PFS; Crane et al. 2006, 2008, 2010) mounted on the 6.5 m
Magellan II Clay Telescope at Las Campanas Observatory
(LCO) in Chile. The observations were performed in 9 dif-
ferent nights, between 18 February and 11 October 2019.
For these observations we used the 0.3″×2.5″ slit, which
delivers high-resolution spectra with a resolving power of
$R = 130\,000$. The observing strategy consisted of obtaining
two consecutive 1200-sec spectra per night of TOI-421 to in-
crease the total S/N ratio per epoch and also to average out
the stellar and instrumental jitter. These observations were
performed with the use of an iodine cell for determining the
radial velocity of the star. The PFS data were processed with
a custom IDL pipeline that is capable of delivering RVs with
a precision less than 1 m s^{-1} (Butler et al. 1996). Addition-
ally, 3 consecutive 1200-sec iodine-free exposures of TOI-
421 were obtained to construct a stellar spectral template for
computing the RVs. The PFS RVs are listed in Table 7.

3. STELLAR PARAMETERS

The fundamental stellar parameters of TOI-421 were
independently determined by two different spectroscopic
methods – one based on spectral synthesis and the other
on template matching – and different sets of isochrones, as
described in the paragraphs below. For this purpose, we uti-
lized the co-added HARPS spectrum, which has a S/N ratio
of ~700 per pixel at 5500 Å.

Method 1. We derived the effective temperature $T_{\rm eff}$, sur-
face gravity $\log g_\star$, iron abundance [Fe/H], and projected
rotational velocity $v \sin i_\star$ with the spectral analysis pack-
age Spectroscopy Made Easy (SME, version 5.2.2; Valenti
& Piskunov 1996; Piskunov & Valenti 2017). We used
the ATLAS12 model spectra (Kurucz 2013) and the line
lists from the Vienna Atomic Line Database[4] (Ryabchikova
et al. 2015) to model the co-added HARPS spectrum. Fol-
lowing the modelling procedure detailed in Fridlund et al.
(2017) and Persson et al. (2018), we measured $T_{\rm eff}$ from
the wings of H-α line, and $\log g_\star$ from the line wings of

the Ca and Mg triplets around 6100 Å and 5100 Å, respec-
tively. $v \sin i_\star$ and [Fe/H] were derived from narrow un-
blended iron lines between 6000 and 6600 Å. The micro- and
macro-turbulent velocities, $v_{\rm mic}$ and $v_{\rm mac}$, were kept fixed us-
ing the Bruntt et al. (2010) and Doyle et al. (2014) calibration
equations for Sun-like stars to 0.9 km s^{-1} and 2.5 km s^{-1},
respectively. The final best fitting model spectrum was
checked using the Na doublet at 5888 Å and 5895 Å.
We found $T_{\rm eff} = 5194 \pm 60$ K, $\log g_\star = 4.45 \pm 0.05$ (cgs),
[Fe/H] $= -0.04 \pm 0.06$ (dex), and $v \sin i_\star = 1.8 \pm 1.0$ km s^{-1}.
The uncertainties are internal error bars that do not account
for the systematic uncertainties of the atmospheric models.

We measured the visual interstellar extinction ($A_{\rm V}$) along
the line of sight to TOI-421 following the method described
in Gandolfi et al. (2008). Briefly, we built the spectral energy
distribution (SED) of the star from the broadband photome-
try listed in Table 1, and fitted the SED using synthetic mag-
nitudes computed from a low-resolution BT-NextGen model
spectrum (Allard et al. 2012) with the same spectroscopic
parameter as the star. We adopted the Cardelli et al. (1989)'s
extinction law and assumed a total-to-selective extinction ra-
tio of $R_{\rm V} = (A_{\rm V})/E(B - V) = 3.1$. We found that the interstel-
lar extinction along the line of sight is consistent with zero
($A_{\rm V} = 0.03 \pm 0.03$), as expected given the relatively short dis-
tance to the star (~75 pc).

In order to compute the stellar mass, radius, and age we
employed the Bayesian PARAM 1.3[5] model tool tracks (da
Silva et al. 2006) with the PARSEC isochrones (Bressan et al.
2012). Input parameters are $T_{\rm eff}$ and [Fe/H] from SME, the
apparent visual magnitude, and the parallax (Table 1). We
added 0.1 mas in quadrature to the parallax uncertainty of
0.0361 mas to account for systematic errors of *Gaia*s as-
trometry (Luri et al. 2018). The resulting stellar parame-
ters are $M_\star = 0.86 \pm 0.02 \, M_\odot$, $R_\star = 0.86 \pm 0.02 \, R_\odot$,
$\log g_\star = 4.48 \pm 0.02$ (cgs), and an age of 9.2 ± 2.3 Gyr. We
note that the derived $\log g_\star$ is in very good agreement with
the spectroscopic value.

Method 2. We used SpecMatch-Emp (Yee et al. 2017)
to analyze the co-added HARPS spectrum via compari-
son with a spectroscopic library of well-characterized stars,
enabling empirical estimates of the effective temperature,
stellar radius, and photospheric iron content. Follow-
ing the procedure described in Hirano et al. (2018) to
adapt the HARPS spectrum for use with SpecMatch-Emp,
we obtained $T_{\rm eff} = 5337 \pm 110$ K, $R_\star = 0.972 \pm 0.100 \, R_\odot$, and
[Fe/H] $= 0.05 \pm 0.09$ dex.

We computed a set of uniformly inferred stellar param-
eters using isochrones (Morton 2015) and MIST (Choi
et al. 2016) to fit 2MASS *JHKs* photometry (Skrut-

---

[4] http://vald.astro.uu.se.
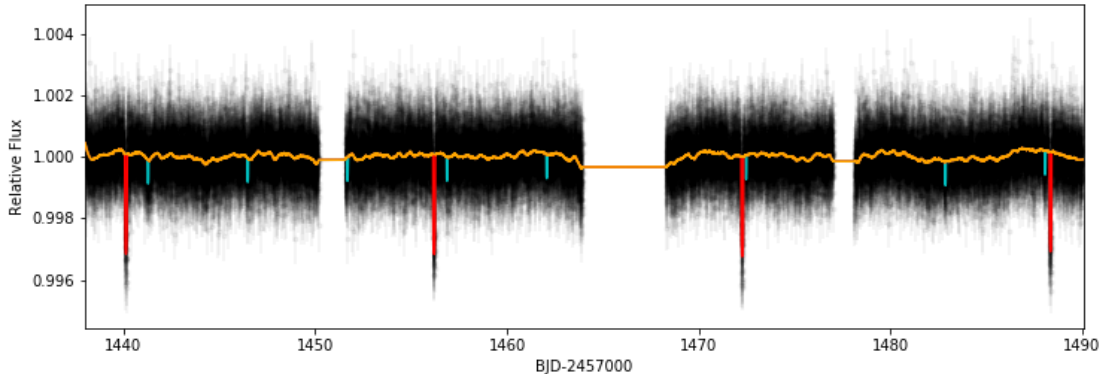
[5] http://stev.oapd.inaf.it/cgi-bin/param_1.3.

Figure 1. *TESS* PDCSAP light curve of TOI-421 is denoted by the black points. The orange line shows the variability filter applied by the transit search algorithm. The detected transits of the 16.1 d planet and the 5.2 d planet are shown in red and cyan, respectively.

skie et al. 2006) and *Gaia* DR2 parallax (Gaia Collaboration et al. 2016, 2018a), adding 0.1 mas of uncertainty in quadrature to account for systematics (Luri et al. 2018). We assumed priors on $T_{\rm eff}$ and [Fe/H] based on the spectroscopic results from SME, using a more conservative prior width of 100 K for $T_{\rm eff}$ to account for systematic errors, and sampled the posterior using MULTI-NEST (Feroz et al. 2013). We obtained the following parameter estimates: $T_{\rm eff} = 5325^{+78}_{-58}$ K, $\log g_\star = 4.486^{+0.025}_{-0.018}$, [Fe/H] = -0.02 ± 0.05 dex, $M_\star = 0.852^{+0.029}_{-0.021}$ M$_\odot$, R$_\star = 0.871\pm 0.012$ R$_\odot$, age = $9.4^{+2.4}_{-3.1}$ Gyr, distance = 74.94 ± 0.58 pc, and A$_{\rm V} = 0.11^{+0.12}_{-0.08}$.

We note that the stellar parameter estimates obtained using the two independent methods agree well within 1-1.5 σ, and serve to ensure the accuracy of our results. While we have no reason to prefer one method over the other, we adopted the results of *Method 2* and list the final adopted parameter estimates in Table 1. The quoted projected rotational velocity $v \sin i_\star$ has been derived following *Method 1*, since *Method 2* does not provide it. The spectroscopic parameters of TOI-421 translate into a spectral type and luminosity class of G9 V (Pecaut & Mamajek 2013).

We also looked for solar-like oscillations (García & Ballot 2019) using an optimized aperture for asteroseismology (González-Cuesta et al. in prep.) for both sectors. While the probability of detection computed following Schofield et al. (2019) is very low for this star, we applied the A2Z pipeline (Mathur et al. 2010) on the concatenated light curves of sectors 5 and 6. Some excess of power and periodicity of the modes (also known as the large frequency separation) was found around 2000 μHz and 3000 μHz but with very low confidence level. The expected frequency of maximum power being around 3500 μHz and the signal-to-noise ratio being still very low, the seismic analysis is not conclusive.

4. *TESS* PHOTOMETRIC ANALYSIS AND PLANET DETECTION

The detection of a 16-day transit signal was issued by the TESS Science Office QLP pipeline in Sector 5, and subsequently identified in the SPOC pipeline (Twicken et al. 2018) in the Sector 6 data set. The SPOC Data Validation difference image centroid offsets for TOI-421 in the multi-sector run indicated that the source of the transit signature was within 1.4″ of the proper motion corrected location of the target star. The detection was then released as a planetary candidate via the TOI releases portal[6] on 08 February 2019. We independently performed transit searches on the PDCSAP light curve using the DST algorithm (Cabrera et al. 2012). The variability in the light curve was filtered using the Savitzky-Golay method (Savitzky & Golay 1964; Press et al. 2002), and a transit model described by a parabolic function was used for transit searches. The algorithm recovered the detection of TOI-421 b where the transit signal has a period of 16.069 ± 0.002 d, a transit depth of 2735.90 ± 76.04 ppm and a duration of 2.72 ± 0.05 hours.

The detection of a 5.2-day signal in the follow-up RV data (see Section 6), prompted further analysis of the *TESS* light curve. The DST algorithm further detected a transit signal with a period of 5.197 ± 0.003 d, a depth of 654.21 ± 88.70 ppm and a duration of 1.23 ± 0.14 hours. The detection of both transit signals were also confirmed with the software package EXOTRANS (Grziwa & Pätzold 2016), which applies the Box least-squares algorithm (BLS; Kovács et al. 2002) for transit searches. Figure 1 shows the PDCSAP light curve of TOI-421 along with the detection of the two planets.

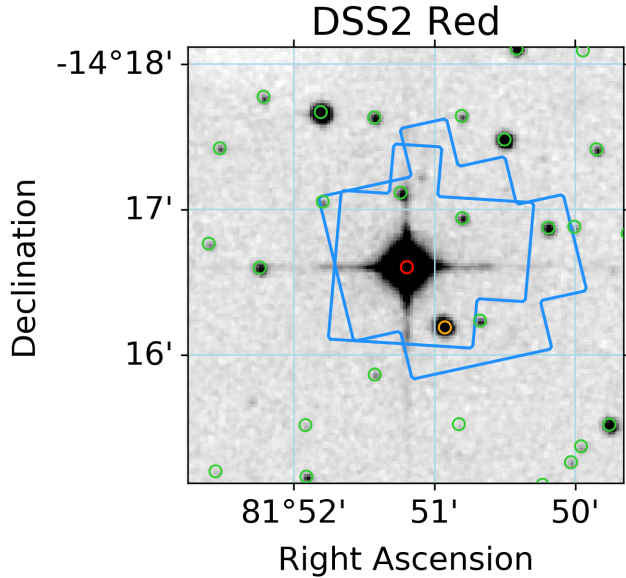## 5. CONTAMINATION FROM POSSIBLE STELLAR COMPANIONS

---

[6] https://tess.mit.edu/toi-releases/.

Figure 2. $3' \times 3'$ DSS2 (Red filter) image with the Sectors 5 and 6 SPOC photometric apertures overplotted in blue. Colored circles denote the positions of *Gaia* DR2 sources within $2'$ of TOI-421; the red circle is TOI-421 (2984582227215748864), the orange circle is a likely bound M dwarf companion (2984582227215748224), and other sources are in green. We computed the contamination from the companion and other stars contributing flux to the aperture, but it is insignificant at $1.8 \pm 0.4\%$ (and consistent with the TIC contamination ratio of 0.024605, see Section 2).

We visually inspected archival images and compared the positions of *Gaia* DR2 (Gaia Collaboration et al. 2018b) sources with the SPOC photometric apertures from Sectors 5 and 6, permitting us to check if the signal could arise from another source, as well as to assess the dilution level of TOI-421. We used the coordinates of TOI-421 from the *TESS* Input Catalog[7] (Stassun et al. 2018) to retrieve *Gaia* DR2 sources and a $3' \times 3'$ image from DSS2[8]. Following the procedures described in Gandolfi et al. (2019) we computed a photometric dilution level of $1.8 \pm 0.4\%$ for TOI-421, which is a little smaller than the SPOC contamination ratios of 0.028 and 0.024 in Sectors 5 and 6, respectively. This small difference is most likely due to the fact that the SPOC target star is affected by an artefact in the 2MASS catalog caused by a diffraction spike from the 2MASS telescope secondary spider. In our specific case this creates a TICv8 neighbor 6.9″ North of the target star, which does not exist. We note that our dilution calculation is not affected by this issue because it is based on *Gaia* DR2.

We discovered that the nearby fainter star, spatially located at ~29.4″ NW of TOI-421 (*Gaia* ID 2984582227215748224,
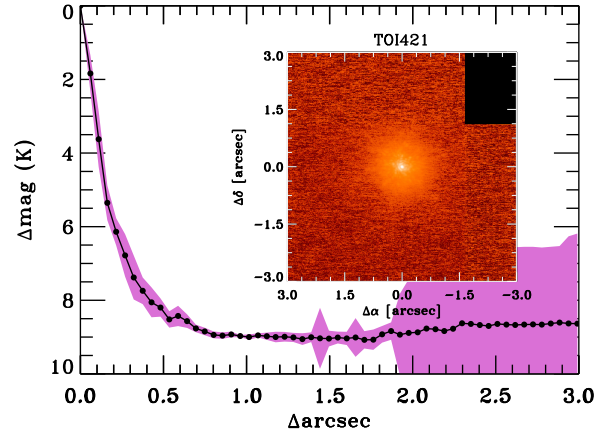
Figure 3. Companion sensitivity for the Keck adaptive optics imaging. The black points represent the 5σ limits and are separated in steps of 1 FWHM ($\sim 0.053''$); the purple represents the azimuthal dispersion (1σ) of the contrast determinations (see text). The inset image is of the primary target showing no additional companions to within $3''$ of the target.

$\Delta G = 4.8$, indicated by an orange circle in Figure 2), has a parallax and *Gaia* G-band extinction that are consistent within the error bars with those of TOI-421, and that two stars have similar proper motions. We concluded that the pair forms very likely a visual binary and TOI-421 is the primary component. According to *Gaia* DR2 effective temperature ($T_{\mathrm{eff}} = 3676^{+376}_{-385}$ K), the secondary component is an M dwarf. The angular separation and parallax imply a separation between the two stars of about 2200 AU.

The Keck AO observations show no additional stellar companions were detected to within a resolution $\sim 0.053''$ FWHM (Figure 3). The sensitivities of the final combined AO image were determined by injecting simulated sources azimuthally around the primary target every $45°$ at separations of integer multiples of the central source's FWHM (Furlan et al. 2017). The brightness of each injected source was scaled until standard aperture photometry detected it with 5σ significance. The resulting brightness of the injected sources relative to the target set the contrast limits at that injection location. The final 5σ limit at each separation was determined from the average of all of the determined limits at that separation; the uncertainty on the 5σ limit was set by the rms dispersion of the azimuthal slices at a given radial distance. The sensitivity curve is shown in Figure 3 along with an inset image zoomed to primary target showing no other companion stars.

In order to measure the likelihood of undetected companions that may cause the planetary radius to be underestimated, we have simulated 10,000 potential stellar companions, drawn from the mass ratio and period distributions presented in Raghavan et al. (2010) and using a method out-
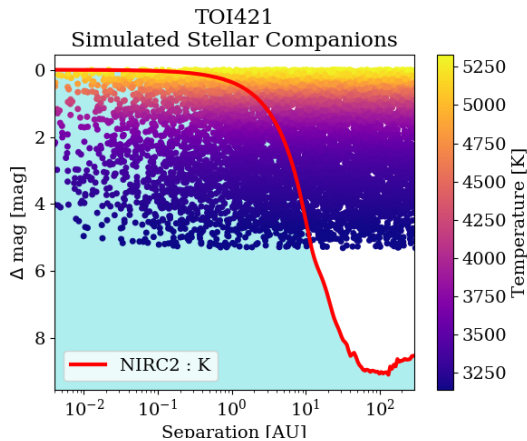
Figure 4. The red line shows the sensitivity curve from NIRC-2 AO observations in the K-band. 10,000 simulated companions are generated, and projected separation and K-band magnitude are calculated. Any companions that lie above the sensitivity curve should be detected in the AO image.

Figure 5. X_R represents the true planet radius over the observed planet radius when considering the impact of dilution of the transit depth from undetected stellar companions. The most likely system is a single-star system and a correction of 1, but the mean correction factor caused by undetected stellar companions is 1.065.

lined more completely in Lund et al (in prep). These companions are then placed at random points in their orbits and projected separations are calculated. We compare the magnitude difference for each potential stellar companion to the sensitivity curve generated from the AO imaging, with any stellar companions that fall above the sensitivity curve being considered detectable, as shown in Figure 4. We find that 77% of the potential stellar companions would be detected, which corresponds to about 13% chance that TOI-421 has an undetected companion. We can also look at the impact that any undetected stellar companions will have on the measured planet radius by looking at the correction factor X_R, defined as the true planet radius over the observed planet radius (Ciardi et al. 2015). For TOI-421, the mean correction factor is 1.065 (Figure 5).

6. FREQUENCY ANALYSIS OF THE HARPS DATA AND STELLAR ACTIVITY

In order to search for the Doppler reflex motion induced by the 16-day transiting planet candidate and unveil the presence of possible additional signals induced by other orbiting planets and/or stellar activity, we performed a frequency analysis of the RV measurements, as well as of the Ca II activity index ($\log R'_{HK}$) and CCF asymmetry indicators (FWHM and BIS). To this aim, we used only the HARPS measurements, as they form the largest homogeneous data-set among our spectroscopic data, and analyzed only the 98 HARPS measurements collected between August 2019 and January 2020, to avoid the presence of spurious peaks associated to the 1-year sampling in the power spectrum of the HARPS time series.

The generalized Lomb-Scargle periodogram (Zechmeister & Kürster 2009) of the 98 HARPS RVs taken between August 2019 and January 2020 displays a significant peak at
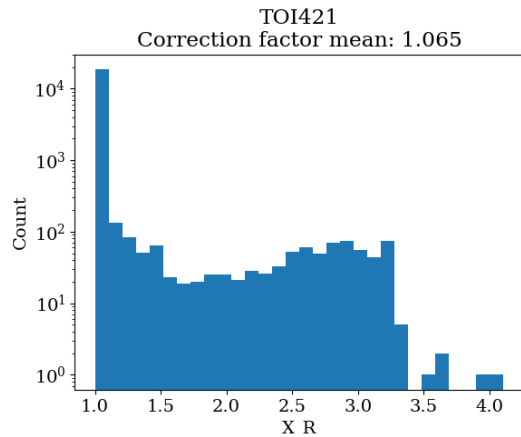
the frequency of the transit signal reported by the *TESS* QLP pipeline ($f_b \approx 0.062\,\mathrm{d}^{-1}$). Following the bootstrap method (Murdoch et al. 1993; Hatzes 2016), we assessed its false alarm probability (FAP) by computing the GLS periodogram of 10^5 mock time-series obtained by randomly shuffling the Doppler measurements and their uncertainties, while keeping the time-stamps fixed. We found that the peak at f_b has a FAP $\ll 0.1$ %. We note that the periodogram of the Ca II activity index $\log R'_{HK}$, as well as those of the CCF asymmetry indicators (FWHM and BIS) do not show any significant peak at f_b (Fig. 6, fourth, fifth and sixth panels), providing strong evidence that this Doppler signal is due to the stellar reflex motion induced by the transiting planet TOI-421 b detected in the *TESS* light curve.

The periodogram of the 98 HARPS RVs shows also a significant peak (FAP<0.1 %) at $f_c \approx 0.193\,\mathrm{d}^{-1}$ ($P_c = 5.2$ d) whose power increases once the Doppler signal of TOI-421 b is removed[9] (Fig. 6; first and second panel). This second peak has no counterpart in the periodograms of $\log R'_{HK}$, FWHM, and BIS, indicating that it is not due to stellar activity. A re-analysis of the *TESS* light curve unveils the presence of a transit signal at 5.2 d, as described in Section 4, confirming that the Doppler signal discovered in the RV time series is associated to a second transiting planet (TOI-421 c).

The periodogram of the RV residuals following the subtraction of the Doppler signal induced by TOI-421 b

---

[9] We removed the Doppler signal of TOI-421 b from the HARPS RVs by fitting a circular model, fixing period and time of first transit to the *TESS* ephemeris, while allowing for the systemic velocity and RV semi-amplitude to vary.
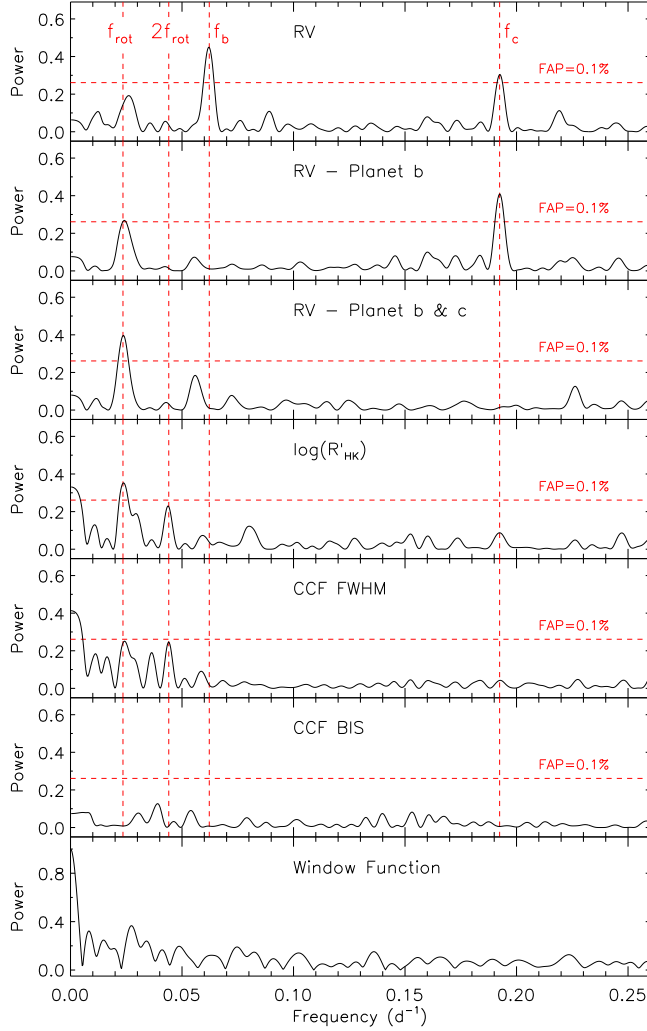
Figure 6. Generalized Lomb-Scargle periodogram of the 98 HARPS measurements acquired between August 2019 and January 2020 (upper panel) and RV residuals, following the subtraction of the Doppler signals of planet b (second panel), and planets b & c (third panel). The periodogram of the Ca II H & K lines activity indicator $\log R'_{HK}$, of the FWHM BIS and BIS, and of the window function are shown in the last four panels. The horizontal dashed lines mark the false alarm probability at 0.1 %. The orbital frequencies of planet b ($f_b \approx 0.062\,d^{-1}$) and c ($f_c \approx 0.193\,d^{-1}$), as well as the stellar rotation frequency ($f_{rot} \approx 0.024\,d^{-1}$) and its first harmonic ($2f_{rot} \approx 0.047\,d^{-1}$) are marked with vertical dashed lines.

(Fig. 6; second panel) shows also a second significant peak[10] (FAP<0.1 %) at $f_{rot} = 0.024 \pm 0.003\,d^{-1}$, corresponding to a period of $P_{rot} = 42\,^{+6}_{-5}$ d and an RV semi-amplitude variation of $\sim 2.4\ m\,s^{-1}$, whose power becomes stronger once the Doppler signal of TOI-421 c is also removed (third panel). This peak is also significantly detected in the GLS peri-

---

Figure 7. Simulated photometric and spectroscopic effects induced by activity regions with radius 0.12 $R_\star$ and located at a stellar latitude of 30°. The upper panel shows the results for a spot with $\Delta T = 663K$ with respect of the quiet photosphere of TOI-421. The lower panel shows the same effects for a plage with $\Delta T = 251K$.

odogram of $\log R'_{HK}$ (FAP < 0.1 %; fourth panel). It is also found in the periodogram of the FWHM (fifth panel), although with a higher false alarm probability (FAP ≈ 0.2 %). This suggests that the rotation period of the star is close to ~42 days and that the third Doppler signal at f_{rot} is induced by intrinsic stellar variability associated with the presence of active regions rotating on and off the visible stellar disk. We note that the periodograms of $\log R'_{HK}$ and FWHM (Figure 6, fourth and fifth panels) display also a peak at the first harmonic of the rotation period ($2f_{rot}$), which is likely due to the presence of active regions at opposite stellar longitudes.

In order to further investigate the nature of the ~42-day signal, we searched the WASP-South data (Section 2.2.2) for any rotational modulation using the methods from Maxted et al. (2011). We found no significant periodicity, with a 95%-confidence upper limit on the amplitude of 1 mmag. We did find a significant periodicity compatible with the lunar cycle, but this was seen only in the data from the 85-mm lenses, which are more vulnerable to moonlight, and not in the 200-mm data; furthermore, in the 85-mm data the same signal was also seen in adjacent field stars, so we concluded that it is not intrinsic of TOI-421.

With a mean $\log R'_{HK}$ of -4.93 ± 0.04 (Table 4), TOI-421 is a relatively quiet star. The lack of significant rotational modulation in the WASP-South light curve might be explained

---

[10] We estimated the uncertainty from the width of the peak by fitting a Gaussian function.

if the spot-induced variability of TOI-421 is too low to produce a photometric signal with an amplitude higher than the WASP-South photometric precision. We further investigated this scenario with the code SOAP2.0 (Dumusque et al. 2014), which simulates stellar activity using a fine grid to model the photosphere of a spotted rotating star. For each grid cell, SOAP2.0 simulates the local CCF using as a reference the solar HARPS CCF, and accounts for the contribution of spots and plages using the HARPS CCF of a solar active region. The adoption of of the solar CCF is an advantage for our test, because TOI-421 is a G9 star, meaning that it is more likely to behave as our Sun. For a given set of stellar parameters and spots/plages distribution, size, and temperature, SOAP2.0 can estimate the photometric and Doppler signals induced by active regions, accounting for the inhibition of the convective blue-shift and limb darkening/brightening effects.

For TOI-421 we used the effective temperature $T_{\rm eff}$ and stellar radius $R_\star$ listed in Table 1, and assumed a rotation period of $P_{\rm rot} = 42$ days. To account for the wavelength range covered by the HARPS spectra, we adopted the linear and quadratic limb darkening coefficients of the Sun ($q_1 = 0.29$ and $q_2 = 0.34$; Claret & Bloemen 2011). Assuming a simplified model with one single spot, we found that the $\sim$2.4 m s^{-1} RV semi-amplitude variation induced by stellar activity could be accounted for by a typical sunspot, with a temperature contrast with respect to the quiet photosphere of $\Delta T = 663$ K (Meunier et al. 2010), a radius of $0.10\,R_\star$ and placed at a latitude of 30°, which is the average active latitude for the Sun (Donati & Landstreet 2009; Strassmeier 2009). The corresponding photometric variation would have an amplitude of 5000 ppm, equivalent to $\sim$ 5 mmag, which is higher than the 1 mmag upper limit of the WASP-South time-series of TOI-421. We performed a similar test by replacing the spot with a plage. We assumed a temperature contrast of $\Delta T = 251$ K (typical plage contrast for the Sun; Meunier et al. 2010) and a radius of $0.12\,R_\star$, while we kept latitude identical to that of the spot (30°). While the resulting RV semi-amplitude is $\sim$2.4 m s^{-1} the photometric variation is 500 ppm, which corresponds to $\sim$0.5 mmag, i.e., lower than the 1 mmag upper limit on the amplitude observed in the WASP-South photometry. In Figure 7, we show the results of our simulations. The upper panel displays the effect of the simulated spot on both the RV and the photometric signal, whereas the bottom panel shows the same for a plage. The photometric effect induced by a plage is thus one order of magnitude smaller than that caused by a spot. These results agree with those reported in Dumusque et al. (2014) and, more recently, by Shapiro et al. (2016) and Milbourne et al. (2019)

To understand if the Doppler signal of TOI-421 is spot- or plage-dominated, we produced an average contour map of the HARPS CCF residuals (after the division for the average CCF), plotted versus radial velocity and stellar rota-
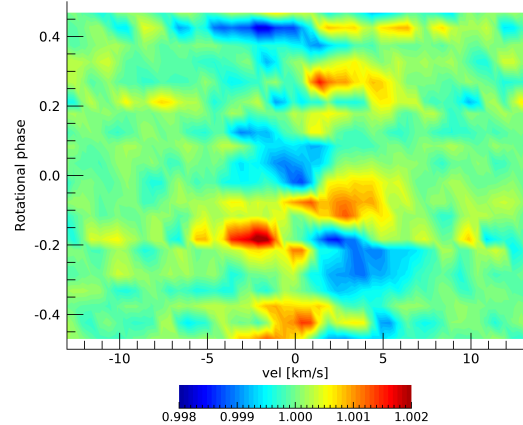

Figure 8. Contour map of the CCF residuals of TOI-421 versus radial velocity and rotational phase. The color bar indicates the variation with respect to the mean CCF.

tion phase. The results are displayed in Figure 8. Positive deviations (i.e., cool star spots) are shown in red, while negative deviations (hot spots) are shown in blue. These can account for the RV variation due to stellar activity, if we consider their associated perturbation to be $\Delta RV \simeq 2 \times {\rm FWHM} \times \Delta I \times f \simeq 14 \times f$, where $\Delta I \sim 0.004$ is the intensity range and $f \leq 1$ the filling factor (Carleo et al. 2020). The contours show that the activity of the star is dominated by plages, though some spots are also evident.

We conclude that the activity-induced Doppler signal of TOI-421 can be explained by plages that would also account for the non detection of any photometric variability in the WASP-South time-series. Alternatively, the star was photometrically quieter at the time of the WASP-South observations (2008-2015) and more active during our spectroscopic follow-up (2019-2020). This is corroborated by the fact that the contour map of the HARPS CCF shows also the presence of spots.

We also analyzed the *TESS* data to look for surface rotation modulation in the light curve due to the passage of spots or active regions on the visible disk. We did the analysis with two different light curves. The first one is the one described in Section 2.1 and the second one is the one optimized for asteroseismology following González-Cuesta et al., in prep. The optimized aperture was obtained by selecting larger and larger apertures with different thresholds in the flux starting from the SPOC aperture (the smaller one) up to the larger one with a threshold of 10e-/s with increments of 10e-/s. In the resultant light curve only points with a quality flag equal to zero have been retained. Missing points have been interpolated using inpainting techniques as in García et al. (2014a). The light curve has also been corrected from outliers and stitched together following García et al. (2011). The optimization is done by comparing the signal measured

at the expected region for the modes (around $3500\,\mu$Hz, Section 3) and the high-frequency noise above $2000\,\mu$Hz. The best aperture found was the one with a threshold of 80 e-/s for sector 5 and a threshold of 10 e-/s for sector 6. For both light curves we removed the transits and concatenated them. Then we applied our rotation pipeline following García et al. (2014b), Mathur et al. (2014), and Santos et al. (2019). Our methodology consists of performing a time-frequency analysis with wavelets, computing the auto-correlation function (ACF) and a composite spectrum (CS) that is a combination of the first 2 methods (see Ceillier et al. 2017). We found a signal at 45 ± 3.54 days in the three methods. The heights of the ACF and CS are above the thresholds defined in Ceillier et al. (2017) to reliably select a rotation period. However, we usually require that we observe 3 rotation periods to have more reliability on the rotation period. With only 58 days of observations we cannot not fulfill this criteria. However, having this period obtained with these 3 different methods and using 2 different processing of the light curves (in terms of apertures) suggests that this period could be from stellar origin and it is independent on the processing of the light curve or the aperture selected. Because the HARPS RV analysis also finds a rotation period of ~42 days, it gives more weight on it being real and the analysis of *TESS* data complements the spectroscopic analysis. Indeed with the *TESS* photometry alone we could not be confident enough about the period found as it could still be a harmonic of a longer periodicity or still something of instrumental origin.

7. RV MODELING

Motivated by the results of our frequency analysis, we performed a series of fits to the RV data to enable model selection and obtain system parameter estimates. Specifically we used RadVel [11] (Fulton et al. 2018) to test six different two-planet models: circular orbits ("2c"), eccentric orbits ("2e"), circular orbits with a Gaussian Process (GP) noise model ("2cGP"), eccentric orbits with a GP noise model ("2eGP"), circular orbits with an additional sine curve for the stellar activity ("2cS"), and eccentric orbits with an additional sine curve for the stellar activity ("2eS"). We used a GP model with a quasi-periodic kernel, which has been used extensively in the literature to model stellar RV signals (see, e.g., Haywood et al. 2014; Grunblatt et al. 2015; Dai et al. 2017); to avoid over-fitting we imposed wide Gaussian priors on the hyper-parameters loosely informed by our frequency analysis.

To compare the quality of these models, we computed both the commonly used Bayesian Information Criterion (BIC) and the Akaike Information Criterion (AICc; corrected for small sample sizes), which is a second-order estimator of

[11] https://github.com/California-Planet-Search/radvel.

Table 2. RV model selection.

Model	AICc	BIC	N_{free}	N_{data}	RMS[a]	$\ln \mathcal{L}$[b]
2eS	587.83	633.88	19	123	2.25	-260.96
2cS	591.48	629.18	15	123	2.38	-268.33
2eGP	596.78	644.79	20	123	1.57	-267.24
2cGP	601.06	640.92	16	123	1.69	-275.19
2c	630.25	661.16	12	123	2.78	-282.70
2e	634.49	674.36	16	123	2.71	-279.66

[a] Root mean square of the data minus the model.

[b] Log-likelihood of the data given the model.

information loss. The results of these fits are presented in Table 2, sorted in ascending order of AICc (best to worst). The 2eS model is strongly favored over the other models by the AICc, suggesting that the orbits of the two transiting planets are significantly eccentric and that the stellar activity is reasonably well described by a sinusoid. We note that the BIC presents a slight preference for the 2cS model, but the AICc has been suggested to have practical advantages over the BIC (Burnham & Anderson 2004). We performed a full MCMC exploration of the parameter space of the 2eS model using RadVel, yielding semi-amplitudes of $K_b = 3.05^{+0.35}_{-0.34}$ and $K_c = 4.33^{+0.37}_{-0.35}$ m s^{-1} for the planetary components, and 2.52 ± 0.36 m s^{-1} for the stellar component; the eccentricities are significant at the ~2σ level and constrained to $e_b = 0.171^{+0.087}_{-0.086}$ and $e_c = 0.147^{+0.069}_{-0.065}$.

8. JOINT ANALYSIS

We performed a global analysis of our RV and transit data with the open-source code pyaneti (Barragán et al. 2019). Briefly, pyaneti creates posterior distributions of the fitted parameters using a Markov chain Monte Carlo (MCMC) sampling approach.

Transits are modelled following a Mandel & Agol (2002) quadratic limb darkening model, implemented with the parametrization suggested by Kipping (2013). A preliminary fit of the light curve shows that the limb-darkening coefficients are not well constrained for the LCOGT data (we note that the limb-darkening coefficients for the *TESS* data are constrained by data themself). Therefore, we used the code LDTk (Husser et al. 2013; Parviainen & Aigrain 2015) to estimate the limb darkening coefficients corresponding to a star with the stellar parameters presented in Table 1, and the Pan-STARSS Y-band (940 − 1060 nm). We used a Gaussian prior with mean given by the LDTk estimation and a conservative standard deviation of 0.1. We also note that we sampled for the stellar density $\rho_\star$, and recover $a/R_\star$ for each planet using third Kepler's law (for more details see, e.g., Winn 2010). We implemented a Gaussian prior on the stellar density using the stellar mass and radius provided in Section 3 to constrain better the orbit eccentricities (see e.g., Van Eylen & Albrecht
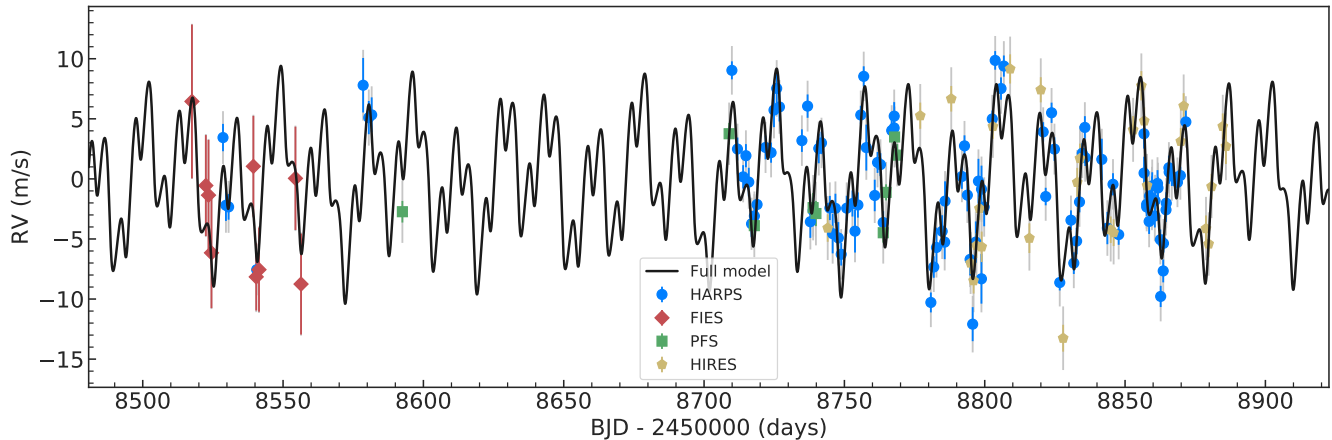
Figure 9. RV time-series. HARPS (blue circles), FIES (red diamonds), PFS (green squares), and HIRES (yellow pentagons) data are shown following the subtraction of the each inferred offset. The inferred full model (i.e. two planet signals plus the activity induced signal) is presented as solid continuous line. Grey error bars account for the inferred jitter for each instrument.

2015). We note that the combination of this transit analysis, together with the RV data, provide a stronger constrain on the orbital eccentricities. The final analysis supports the conclusions of Section 7 (See Table 3).

The RV model was chosen following the results presented in Section 7. We used two Keplerian orbits to model the Doppler reflex motion induced by the two transiting planets, and an extra sinusoidal to take into account the activity signal induced by the star at its rotation period.

We used 500 Markov chains to explore the parameter space. We stopped the sampling once all chains converged (following Gelman & Rubin 1992, we define convergence when $R < 1.02$ for all parameters). The posterior distribution were created using the last 2500 converged iterations and the 500 chains, leading to a posterior of 1,250,000 points per parameter.

Details on the fitted parameters, adopted priors, and parameter estimates are given in Table 3. Inferred parameters are defined as the median and 68% region of the credible interval of the posterior distributions for each fitted parameter. Figure 9 shows the RV model time-series. The phase-folded RV and transit plots are shown in Figures 10 and 11, respectively. We note that there is an apparent shift of ~ 20 min on the LCO transit in Fig. 11. Given that the expected TTVs in the system are smaller (see Section 9.4), it is likely that this effect is caused by systematics in the ground-based data.

9. DISCUSSION

The outer transiting planet, TOI-421 b, ($P_b \approx 16.1$ days) has a mass of $M_b = 16.23^{+1.14}_{-1.08} \; M_\oplus$ and a radius of $R_b = 5.17^{+0.13}_{-0.13} \; R_\oplus$ resulting in a mean density of $\rho_b = 0.645^{+0.069}_{-0.062} \;$ g cm^{-3}. The innermost planet, TOI-421 c, ($P_c = 5.2$ days) has a mass of $M_c = 7.05^{+0.71}_{-0.70} \; M_\oplus$ and a radius of $R_c = 2.72^{+0.19}_{-0.18} \; R_\oplus$, yielding a density of $\rho_c = 1.93^{+0.49}_{-0.39} \;$ g cm^{-3}. Figure 12 shows the position of TOI-421 b and c in the

mass-radius diagram along with the sample of small planets ($R_p \leqslant 6 \, R_\oplus$) whose masses and radii have been measured with a precision better than 20%. Given their positions with respect to theoretical mass-radius relations, both planets are expected to host an atmosphere dominated by light elements, namely H and He. We performed a series of simulations – including hydrogen escape rate (Section 9.1), planetary atmospheric evolution (Section 9.2), and retrievals of the transmission spectrum (Section 9.3) – which indicate that TOI-421 b and c are very intriguing planets for atmospheric characterization. Finally, we compute the Helium 10830 Å simulation following the approach in Oklopčić & Hirata (2018) finding no significant Helium absorption ($\lesssim 0.5\%$ at line center) for either of the two planets.

9.1. *Hydrogen escape*

Atmospheric escape in close-in planets takes place when the high-energy (X-ray+EUV; hereafter XUV) stellar photons photoionize and heat up the planetary upper atmospheres (e.g., Murray-Clay et al. 2009). TOI-421 b's and c's close distances to the star suggest that their atmospheres may be significantly heated by the stellar high-energy emission and hence are undergoing escape. Therefore, these two planets are very appealing objects for studying the effects of mass loss. Interestingly, two other objects with similar bulk densities, that is K2-18b ($M_p = 8.64 M_\oplus$, $R_p = 2.711 R_\oplus$) and GJ3470b ($M_p = 13.9 M_\oplus$, $R_p = 4.8 R_\oplus$), have shown the presence of atmospheric escape through the detection of Ly-α absorption during transit (Bourrier et al. 2018; dos Santos et al. 2020).

Here, we use the 1D hydrodynamic atmospheric escape model presented in Allan & Vidotto (2019) to predict the behaviour of the planetary atmospheres under the influence of the photoionizing flux of the host star. With this we can infer the current properties of the planetary upper atmospheres,

Table 3. TOI-421 parameters.

Parameter	Prior[a]	Value[b]
Model Parameters for TOI-421b		
Orbital period $P_{\rm orb}$ (days)	$\mathcal{U}[16.0642, 16.0741]$	$16.06815^{+0.00034}_{-0.00035}$
Transit epoch T_0 (BJD - 2,450,000)	$\mathcal{U}[8440.0804, 8440.1804]$	$8440.13169^{+0.00071}_{-0.00067}$
$\sqrt{e}\sin\omega_\star$	$\mathcal{U}(-1, 1)$	$0.344^{+0.065}_{-0.094}$
$\sqrt{e}\cos\omega_\star$	$\mathcal{U}(-1, 1)$	$-0.168^{+0.087}_{-0.079}$
Scaled planetary radius $R_{\rm p}/R_\star$	$\mathcal{U}[0, 0.05]$	$0.0545^{+0.0011}_{-0.0011}$
Impact parameter, b	$\mathcal{U}[0, 1]$	$0.75^{+0.028}_{-0.030}$
Radial velocity semi-amplitude variation K (m s^{-1})	$\mathcal{U}[0, 50]$	$4.64^{+0.31}_{-0.29}$
Model Parameters for TOI-421c		
Orbital period $P_{\rm orb}$ (days)	$\mathcal{U}[5.1917, 5.2017]$	$5.19676^{+0.00049}_{-0.00048}$
Transit epoch T_0 (BJD - 2,450,000)	$\mathcal{U}[8441.2335, 8441.3335]$	$8441.2847^{+0.0020}_{-0.0018}$
$\sqrt{e}\sin\omega_\star$	$\mathcal{U}(-1, 1)$	$0.29^{+0.14}_{-0.23}$
$\sqrt{e}\cos\omega_\star$	$\mathcal{U}(-1, 1)$	$-0.2^{+0.14}_{-0.11}$
Scaled planetary radius $R_{\rm p}/R_\star$	$\mathcal{U}[0, 0.05]$	$0.0286^{+0.002}_{-0.0019}$
Impact parameter, b	$\mathcal{U}[0, 1]$	$0.935^{+0.016}_{-0.024}$
Radial velocity semi-amplitude variation K (m s^{-1})	$\mathcal{U}[0, 50]$	$2.94^{+0.28}_{-0.28}$
Model parameters of activity induced RV sinusoidal signal		
Period $P_{\rm rot}$ (days)	$\mathcal{U}[35, 50]$	$43.12^{+0.64}_{-0.61}$
Transit epoch T_0 (BJD - 2,450,000)	$\mathcal{U}[8412.2835, 8452.2835]$	$8431.51^{+5.14}_{-5.40}$
Radial velocity semi-amplitude variation K (m s^{-1})	$\mathcal{U}[0, 50]$	$2.42^{+0.3}_{-0.3}$
Other system parameters		
Stellar density $\rho_\star$	$\mathcal{N}[1.83, 0.10]$	$1.829^{+0.096}_{-0.099}$
Systemic velocity (HARPS, km s^{-1})[c]	$\mathcal{U}[79.0318, 80.0537]$	79.54384 ± 0.00024
Instrumental offset FIES (km s^{-1})[c]	$\mathcal{U}[-0.5, 0.5]$	$-0.017^{+0.0016}_{-0.0015}$
Instrumental offset PFS (km s^{-1})[c]	$\mathcal{U}[-0.5, 0.5]$	0.00222 ± 0.00099
Instrumental offset HIRES (km s^{-1})[c]	$\mathcal{U}[-0.5, 0.5]$	$-0.00056^{+0.00050}_{-0.00052}$
Jitter term $\sigma_{\rm HARPS}$ (m s^{-1})	$\mathcal{U}[0, 100]$	$1.88^{+0.21}_{-0.18}$
Jitter term $\sigma_{\rm FIES}$ (m s^{-1})	$\mathcal{U}[0, 100]$	$0.97^{+1.67}_{-0.74}$
Jitter term $\sigma_{\rm PFS}$ (m s^{-1})	$\mathcal{U}[0, 100]$	$2.47^{+1.13}_{-0.68}$
Jitter term $\sigma_{\rm HIRES}$ (m s^{-1})	$\mathcal{U}[0, 100]$	$2.39^{+0.49}_{-0.39}$
Limb darkening q_1 TESS	$\mathcal{U}[0, 1]$	$0.271^{+0.125}_{-0.084}$
Limb darkening q_2 TESS	$\mathcal{U}[0, 1]$	$0.65^{+0.23}_{-0.35}$
Limb darkening q_1 Pan-STARSS Y-band	$\mathcal{N}[0.24, 0.1]$	$0.156^{+0.104}_{-0.093}$
Limb darkening q_2 Pan-STARSS Y-band	$\mathcal{N}[0.36, 0.1]$	$0.344^{+0.100}_{-0.099}$
Derived parameters for TOI-421b		
Planet mass ($M_\oplus$)	$\cdots$	$16.23^{+1.14}_{-1.08}$
Planet radius ($R_\oplus$)	$\cdots$	$5.17^{+0.13}_{-0.13}$
Planet density (g cm^{-3})	$\cdots$	$0.645^{+0.069}_{-0.062}$
semi-major axis a (AU)	$\cdots$	$0.1182^{+0.0026}_{-0.0027}$
e	$\cdots$	$0.152^{+0.042}_{-0.045}$
$\omega_\star$ (deg)	$\cdots$	$115.4^{+16.5}_{-14.1}$
Orbital inclination i (deg)	$\cdots$	$88.301^{+0.067}_{-0.072}$
Transit duration (hours)	$\cdots$	$2.72^{+0.048}_{-0.040}$
Equilibrium temperature[d] $T_{\rm eq}$ (K)	$\cdots$	$696.6^{+12.3}_{-12.1}$
Insolation $F_{\rm p}$ ($F_\oplus$)	$\cdots$	$39.25^{+2.84}_{-2.65}$
Derived parameters for TOI-421c		
Planet mass ($M_\oplus$)	$\cdots$	$7.05^{+0.71}_{-0.70}$
Planet radius ($R_\oplus$)	$\cdots$	$2.72^{+0.19}_{-0.18}$
Planet density (g cm^{-3})	$\cdots$	$1.93^{+0.49}_{-0.39}$
semi-major axis a (AU)	$\cdots$	$0.0557^{+0.0012}_{-0.0013}$
e	$\cdots$	$0.147^{+0.093}_{-0.084}$
$\omega_\star$ (deg)	$\cdots$	$119.4^{+26.6}_{-35.7}$
Orbital inclination i (deg)	$\cdots$	$85.6^{+0.38}_{-0.49}$
Transit duration (hours)	$\cdots$	$1.115^{+0.065}_{-0.069}$
Equilibrium temperature[d] $T_{\rm eq}$ (K)	$\cdots$	$1014.9^{+17.9}_{-17.6}$
Insolation $F_{\rm p}$ ($F_\oplus$)	$\cdots$	$176.8^{+12.8}_{-11.9}$

Note – [a] $\mathcal{U}[a, b]$ refers to uniform priors between a and b, $\mathcal{N}[a, b]$ to Gaussian priors with median a and standard deviation b, and $\mathcal{F}[a]$ to a fixed value a. [b]. Inferred parameters and errors are defined as the median and 68.3% credible interval of the posterior distribution. [c] HARPS observations are absolute RVs, therefore the instrumental offset correspond to the systemic velocity of the system. Other instruments provide relative RV values. [d] Assuming albedo = 0.
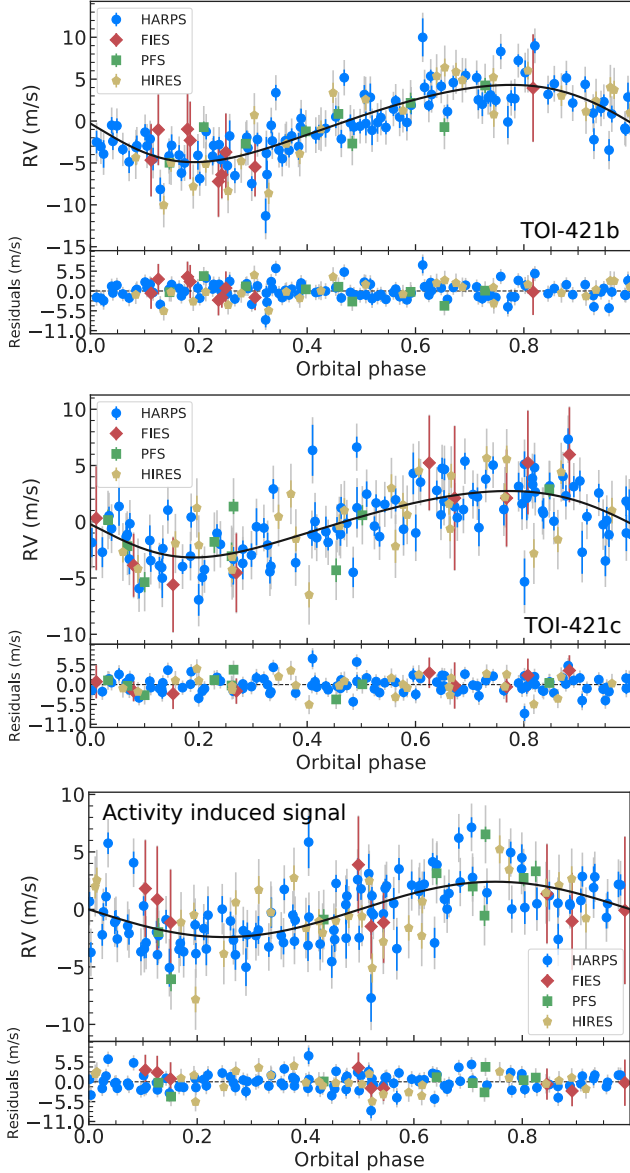
Figure 10. Phase-folded RV plots with residuals for TOI-421b (top panel), TOI-421c (middle panel), and activity induced signal (lower panel). HARPS (blue circles), FIES (red diamonds), PFS (green squares), and HIRES (yellow pentagons) data are shown following the subtraction of the each inferred offset and the other signals. Black solid line shows the inferred model for each case. Grey error bars account for the inferred jitter for each instrument.

including the mass-loss rate. Fro the output of this 1D model we study study the atmospheric signatures of TOI-421 b and TOI-421 c of the neutral hydrogen Ly-α and H-α lines during transit. Our model uses as input the XUV stellar luminosity, which was derived considering the median log R'$_{\rm HK}$ value (-4.93 ± 0.04) from Table 4, converting it into a Ca II H&K chromospheric emission flux using the equations listed in Fossati et al. (2017b) and then by converting this emission in XUV flux using the scaling relations of Linsky et al. (2013)
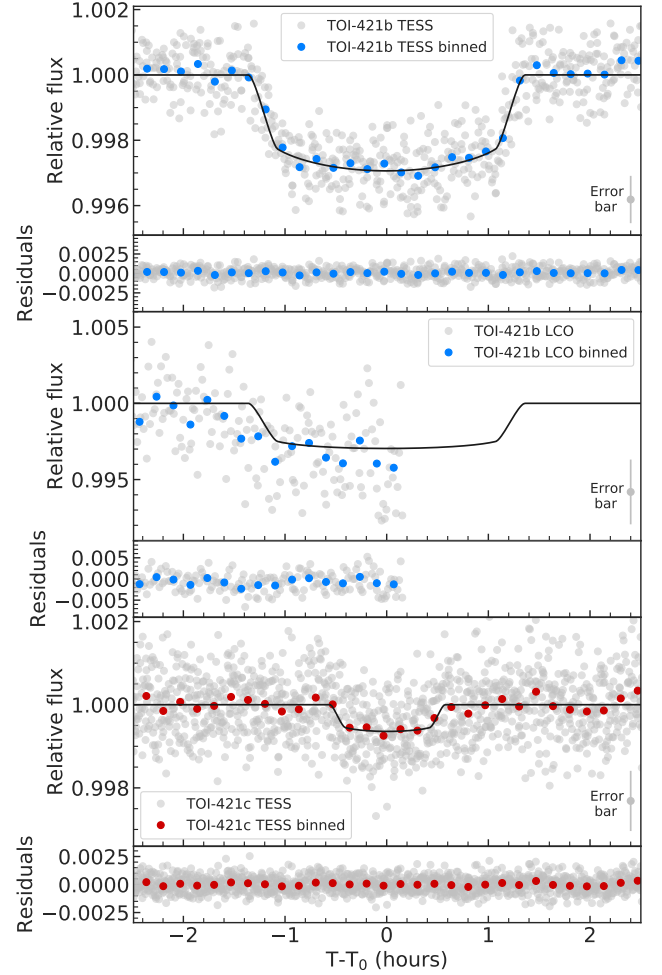
Figure 11. Light curves around the transit with residuals of TOI-421b (upper and middle panels refer to *TESS* and LCOGT, respectively) and TOI-421c (*TESS*, lower panel) with inferred transit model over-plotted. Data are shown in the nominal short-cadence mode and binned to 10 min. Typical error bar for nominal data are shown at the bottom right for each panel.

and Linsky et al. (2014). We find an XUV flux at a distance of 1 AU of $F_{\rm XUV}$ = 23.12 erg cm^{-2} s^{-1}, corresponding to an XUV luminosity of $L_{\rm XUV}$ = 6.5×10^{28} erg s^{-1}. This implies XUV fluxes of $F_{\rm XUV}$ = 1654.8 erg cm^2 s^{-1} and $F_{\rm XUV}$ = 7452.0 erg cm^2 s^{-1} at the distance of planet b and c, respectively.

Figure 13 summarizes some key properties of the escaping atmosphere for both planets: radial component of the velocity (top), temperature (middle) and ionisation fraction (bottom). For planet c (inner planet), we derive an atmospheric escape rate of 4.5×10^{10} g s^{-1}. We calculate the Roche lobe distance to be at $9.7\,R_p$ and, at this distance, the speed of the escaping material is about 30 km s^{-1}. Planet b has a comparable, although slightly smaller, escape rate of 4.4×10^{10} g s^{-1}, with material reaching a speed of 28 km s^{-1} at the Roche lobe distance ($14.3\,R_p$). The reason for comparable escape is
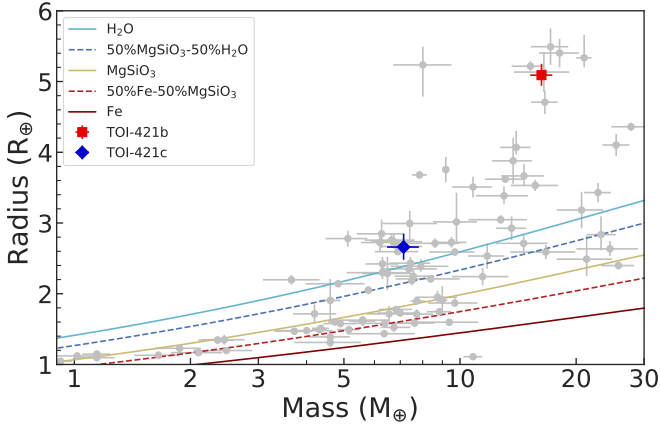
Figure 12. Mass-radius diagram for planets with mass and radius measurement precision better than 20% (gray points, from the TEP-Cat database; Southworth 2011). TOI-421b (red square) and TOI-421(blue diamond) are shown for comparison. Zeng et al. (2016)'s theoretical composition models are shown using different lines and colours.

that, although planet b receives an XUV flux that is 4.5 times smaller than planet c due to its larger orbital distance, it has a lower surface gravity ($g_b \simeq 24\%$ of Jupiter's gravity versus $g_c \simeq 38\%$ for planet c). It is more difficult for low-gravity planets to hold on to their atmospheres, thus the lower gravity of planet b compensates for its lower incident XUV flux, reaching comparable escape to planet c.

In spite of the similarities in the escape rates and velocities, we predict different Ly-α transit absorptions for these two planets. Figure 14 shows the predicted lightcurves at Ly-α line centre, where we see that planet c (the inner planet) shows a maximum absorption of 35% and planet b (the outer planet) shows a maximum absorption of 53%. These different absorptions are caused by the different ionisation fractions in each planet's atmosphere (see bottom panel of Fig. 13), with planet b showing more neutral hydrogen in its atmosphere. The lightcurves presented in Figure 14 are symmetric about mid-transit. This is due to the one-dimensional geometry of the model, hence of the assumption of spherically symmetric planetary atmospheres. However, we expect lightcurves to be asymmetric with respect to mid-transit, but these asymmetries can only be captured by 3D models that include interactions with the stellar wind (e.g., Villarreal D'Angelo et al. 2014, 2018), which we leave to a forthcoming paper.

To encourage future observations in the UV we made use of the absorption profile obtained from the upper atmosphere simulations and computed the expected Ly-α profile as observed with the G140M grating of the STIS spectrograph on board HST. Figure 15 shows the resulting profiles at three different times reproducing an out of transit observation (black line) and an observation at mid-transit of planet b (red-dashed
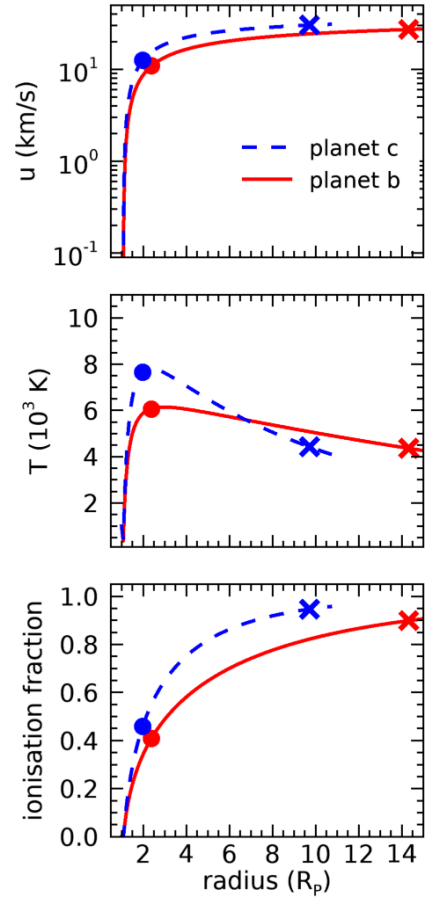

Figure 13. Profiles of hydrodynamic hydrogen escape for planet b (red) and c (blue). From top to bottom: radial velocity of the escaping atmosphere, temperature and ionisation fraction. The dot and the cross indicate the sonic point (when planetary material reaches sound speed) and Roche lobe boundary, respectively.
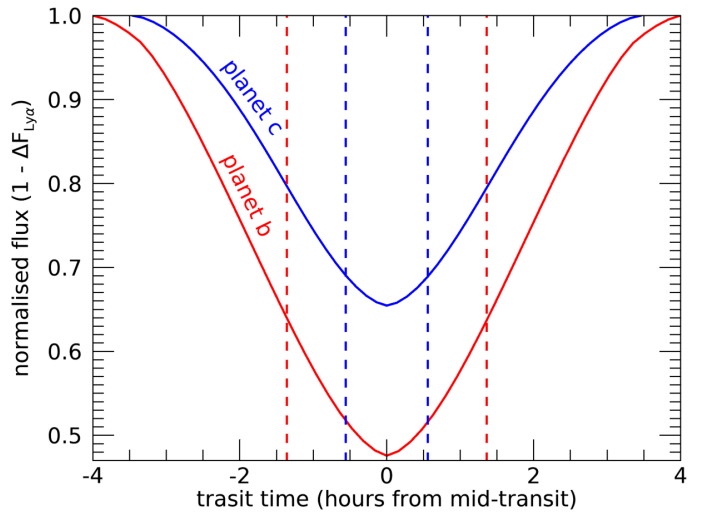

Figure 14. Predicted lightcurves for planet b (red) and c (blue) at the Ly-α line centre. The red and blue vertical dashed lines represent the first and fourth contact points for planet b (red) and c (blue).
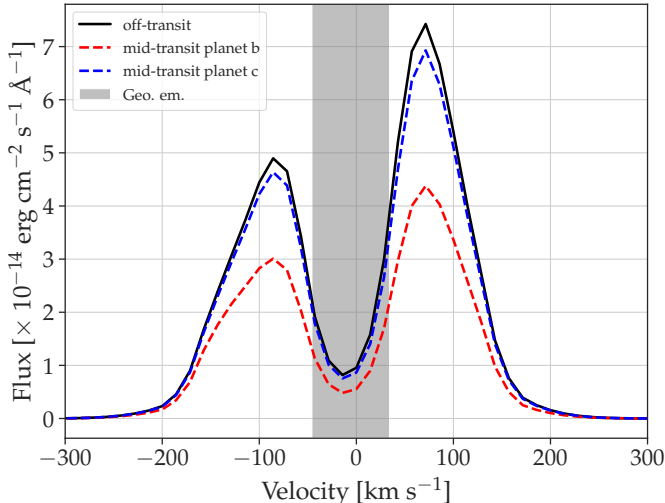
Figure 15. Predicted Ly-α line profile out-of-transit (black line), at mid-transit for planet b (red-dashed line) and at mid-transit for planet c (blue-dashed line) at the spectral resolution of the G140M grating of the STIS spectrograph on board HST. The gray stripe represents the part of the line expected to be contaminated by geocoronal emission.

line) and planet c (blue-dashed line). To compute the out of transit Ly-α profile of TOI-421, we scaled the intrinsic Ly-α profile of ξ Boo A (G8 V, d = 6.70 pc, $R_\star = 0.78\,R_\odot$) derived by Wood et al. (2005). We assumed that the strength of the profiles of the two stars should be similar as the stellar type and activity index for ξ Boo A (log $R'_{HK} \sim -4.40$, Morgenthaler et al. (2012)) are close to those of TOI-421. Most of the predicted absorption will be hidden by the ISM absorption and geocoronal emission as shown in Fig. 15. However, the ISM will affect the spectrum absorbing a significant fraction of its flux beyond almost 100 pc and probably most of it by 200 pc, while TOI-421 is 75 pc distant. Moreover, because of the interaction of the escaping planetary upper atmosphere with the stellar wind and the resolution of the G140M grating, significant planetary Ly-α absorption will be visible in the line wings, making it detectable. The attenuation caused by the ISM over the intrinsic profile of TOI-421 is assumed to be the same as the one estimated for ξ Boo A, also computed in the work of Wood et al. (2005). This is a crude approximation, but a more adequate estimation would require at least a near-ultraviolet observation of the ISM absorption at the position of the MgII h&k lines (Wood et al. 2005). Using HST we expect to be able to detect the absorption signal caused by planet b during transit, as this is the largest absorption modelled, in accordance to what is shown with Fig. 14.

We also compute the H-α transit lightcurves following the approach outlined in Allan & Vidotto (2019). Although we predict a large absorption in Ly-α, no appreciable absorption is expected to be detectable in H-α. This is because

most of the hydrogen in the atmospheres of TOI-421 b and TOI-421 c is in the ground state – for H-α to be formed, it is required some hydrogen in the first excited state. The fact that we do not predict any H-α absorption in our model needs to be reassessed in 3D calculations. Recently, Villarreal D'Angelo et al. (submitted) demonstrated that the interaction between the upper planetary atmosphere and the stellar wind, which is only captured in 3D models, could increase the atmospheric temperature in the interaction zone. As a result, this can increase the number of neutral hydrogen in the first excited state, possibly enhancing H-α absorption. We will further explore this in a future work.

9.2. *Planetary atmospheric evolution*

In addition to the hydrodynamic model presented in Section 9.1, as a cross-check, we also computed the mass-loss rates employing the interpolation routine of Kubyshkina et al. (2018), which is based on 1D hydrodynamic simulations, obtaining a value of 1.6×10^{10} g s^{-1} for planet b and 2.7×10^{10} g s^{-1} for planet c, in agreement with the results obtained using the hydrodynamic atmospheric escape model of Allan & Vidotto (2019). We further notice the low Λ[12] value ($\Lambda = 19.33$) of planet c, which implies that the planetary gravity is hardly capable to hold a hydrogen-dominated atmosphere (Fossati et al. 2017a). In fact, this is remarkable because other planets with similarly low Λ values have an average density indicative of a mostly rocky composition (Gandolfi et al. 2017). This is confirmed by the mass-loss rates of planets b and c that imply that they would have lost 5% and 20%, respectively, of their mass over 1 Gyr. While planet b should have an atmospheric mass fraction large enough to sustain such an intense mass loss over Gyrs, for planet c the escape is probably too intense to be able to still retain a hydrogen-dominated atmosphere, as instead suggested by the average density.

We employed the tool presented by Kubyshkina et al. (2019a,b) to constrain the atmospheric evolution of both planets, their initial atmospheric mass fractions, and the evolution of the rotation rate (and therefore also of the XUV emission) of the host star. In short, the framework mixes three ingredients: a model of the stellar XUV flux evolution (after Pizzolato et al. 2003; Mamajek & Hillenbrand 2008; Wright et al. 2011; Sanz-Forcada et al. 2011), a model relating planetary parameters and atmospheric mass (after Stökl et al. 2015; Johnstone et al. 2015b), and a model computing escape (after Kubyshkina et al. 2018). The framework also accounts for the evolution of the stellar bolometric luminosity, hence planetary equilibrium temperature, using the

---

[12] The parameter $\Lambda = \frac{GM_p m_H}{k_B T_{eq} R_p}$, where m_H is the mass of the hydrogen atom, is the restricted Jeans escape parameter and it is a measure of the thermal escape driven by the intrinsic atmospheric temperature and low planetary gravity (Fossati et al. 2017a).
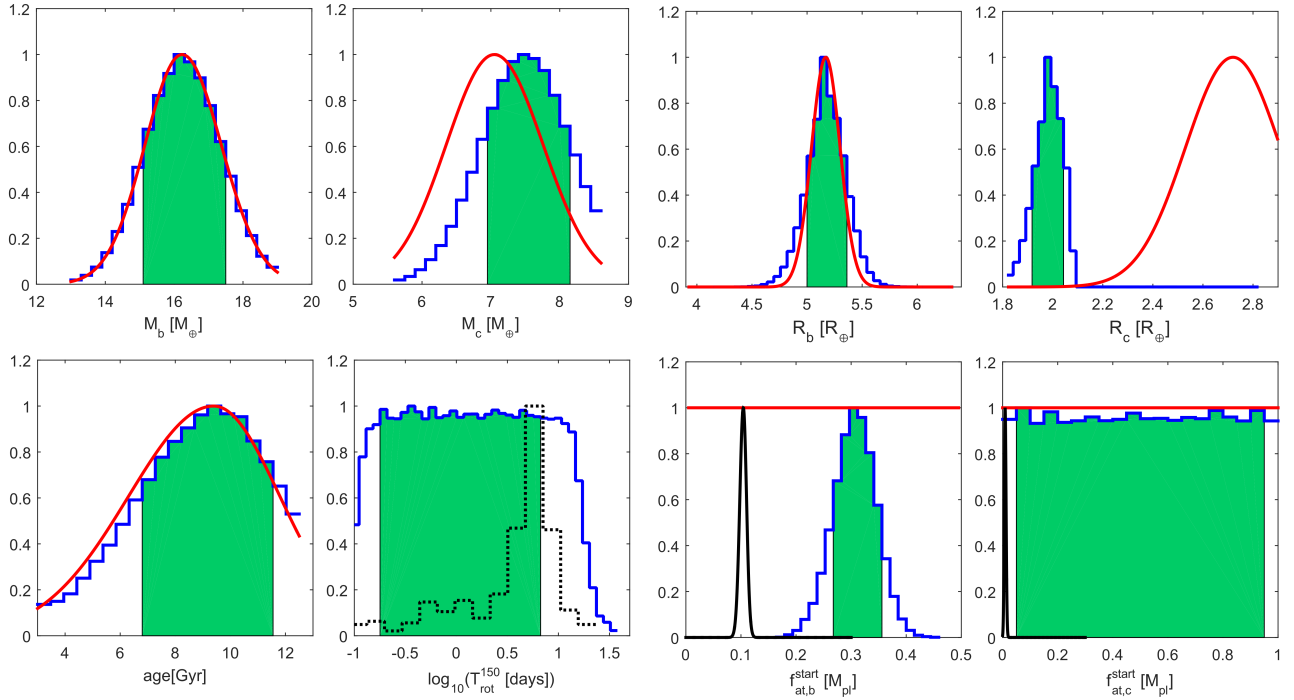
Figure 16. Top, from left to right: posterior probability distribution functions for mass of planet b, mass of planet c, radius of planet b, radius of planet c. Bottom, from left to right: posterior probability distribution function for system's age, stellar rotation period at an age of 150 Myr, initial atmospheric mass fraction for planet b, and initial atmospheric mass fraction for planet c. The blue solid lines indicate the posterior probabilities, the green shaded areas correspond to the 68% HPD credible intervals, and the red solid lines are the priors. The dashed black line in the second-from-left bottom panel shows the distribution measured for solar mass members of ≈150 Myr-old open clusters (Johnstone et al. 2015a). The black solid lines in the two right bottom panels illustrate the present time atmospheric mass fractions obtained for the posteriors given by MCMC.

MESA Isochrones and Stellar Tracks (MIST, Paxton et al. 2018) grid.

For a given core mass, the framework sets the core radius assuming an Earth-like density and the atmospheric mass is considered to be negligible (Owen & Wu 2017). Then, starting at 5 Myr (the assumed age of the dispersal of the protoplanetary disk), at each time step the framework extracts the mass-loss rate from the grid based on the stellar flux and system parameters, using it to update the atmospheric mass fraction and the planetary radius. This procedure is then repeated until the age of the system is reached or the planetary atmosphere is completely escaped. The framework simulates the atmospheric evolution of both planets, simultaneously. The main frameworks assumption is that the analysed planets have (or had) a hydrogen-dominated atmosphere and that the planetary orbital separation does not change after the dispersal of the protoplanetary disk.

The input parameters of the framework are planetary masses, planetary radii, orbital separations, current stellar rotation rate, and stellar mass, while the free parameters are the index of the power law describing the evolution of the stellar XUV flux and the initial planetary radius (i.e., the initial atmospheric mass fraction at the time of the dispersal of the

protoplanetary disk; f_{at}). The input parameters are set equal to the measurements with Gaussian priors having a width equal to the measurement uncertainties, while we take flat priors for the output parameters. The output parameters are constrained by implementing the atmospheric evolution algorithm in a Bayesian framework employing the Markov-chain Monte Carlo (MCMC) tool of Cubillos et al. (2017a).

Figure 16 shows the main results of the simulation. The posteriors on the input parameters of the host star and of the outer planet (TOI-421 b) match the priors. The evolution of the stellar rotation rate (or XUV emission) is mostly unconstrained. For the outer planet, the analysis leads to a rather tight constraint on the initial atmospheric mass fraction of about 30% and this result holds also when running the analysis solely on the outer planet, meaning that the anomaly found for the inner planet (see below) does not affect the other results. The outer planet could not have accreted an atmosphere much larger than $f_{at} \approx 30\%$ while in the disk, because otherwise the stellar XUV emission would have not been able to remove enough of it to obtain the currently observed radius, even if the star was a fast rotator. Similarly, the planet could not have accreted an atmosphere much smaller than $f_{at} \approx 30\%$ while in the disk, because otherwise the stel-

lar XUV emission would have removed too much atmosphere given the observed radius, even if the star was a slow rotator.

The result obtained for the inner planet is extremely interesting. The framework is unable to find a configuration in which the planet is capable of retaining enough atmosphere to match the measured planetary mass, radius, and orbital separation. This is why the posterior of the planetary mass is slightly shifted towards higher masses compared to the prior (second from left, top panel of Fig. 16) and, moreover, the posterior of the planetary radius is significantly shifted towards smaller radii compared to the prior (rightmost, top panel of Fig. 16). In other words, given the system parameters, the framework finds that the inner planet always loses its hydrogen atmosphere, regardless of the evolution of the stellar XUV emission. An inspection of the atmospheric evolutionary tracks indicates that the inner planet is expected to completely lose its atmosphere within 1 Gyr, while the estimated age of the system is significantly larger. We reran the simulation looking for the planetary parameters that would enable the posteriors on mass and radius not to vary from the priors, obtaining either an orbital separation of about twice the measured one (keeping mass and radius equal to the measured values), or a planetary mass of about $16\,M_\oplus$ (keeping radius and orbital separation equal to the measured values), or a planetary radius of about $2\,R_\oplus$ (keeping mass and orbital separation equal to the measured values). In the last two options the planet would not host a hydrogen-dominated atmosphere.

CoRoT-24b was the first planet identified to have a low bulk density, compatible with the presence of a hydrogen-dominated atmosphere, but at the same time to be also subject to a too extreme mass loss for hosting one (Lammer et al. 2016). Cubillos et al. (2017b) analysed the upper atmospheric properties and high-energy irradiation of a large sample of mini-Neptunes, detected mostly by the *Kepler* satellite, finding that 15% of them share this same peculiar property. There is a range of possible solutions to this puzzle. One of the main assumptions in the atmospheric evolution framework is that orbital separations do not change with time following the dispersal of the protoplanetary nebula, which may not be the case, for example, if the system had a close-enough encounter with another star in the past. It may also be that the hydrodynamic model overestimates the mass-loss rates, although past comparisons between observations and hydrodynamic models would tend to exclude orders of magnitude errors in the computed rates. One further possibility is a bias in the measured planetary parameters (mass and/or radius), maybe caused by the presence of other undetected planets in the system biasing the planetary mass measurement, but it seems unlikely, given the quantity and quality of data. The mainstream explanation for this kind of planet is the presence of high-altitude aerosols that would lead overestimation of

planetary radius (Lammer et al. 2016; Cubillos et al. 2017b; Gao & Zhang 2020). Future atmospheric characterisation observations, particularly those at low resolution that are more sensitive to aerosols, will be able to identify whether this is the case or not (e.g., Libby-Roberts et al. 2020). There is also the additional possibility that the crust released a significant amount of light gases in the atmosphere, counteracting the effect of escape (e.g., Kite et al. 2019).

9.3. *Simulated HST WFC3 retrievals*

With its large radius ($\sim 5\,R_\oplus$), TOI-421 b represents an excellent target for atmospheric characterization. TOI-421 c is somewhat more challenging; its scale height is comparable to TOI-421 b, but because c is smaller by a factor of two, so will be the transit signal corresponding to one scale height, similarly as Ly-α absorption. To assess how well the atmospheric parameters of TOI-421 b and c could be derived from observations, we modeled the planetary atmospheres and derived transmission spectra with the open-source `petitRADTRANS` package (Mollière et al. 2019). The atmospheres were set up to be isothermal, at the equilibrium temperature of the planets. The absorber abundances were obtained from assuming chemical equilibrium, calculated with the chemistry module that is part of petitCODE (Mollière et al. 2017). We assumed a solar C/O ratio of 0.55, and two different metallicity values, 3 and $100 \times$ solar (Jupiter and Neptune-like, respectively). We also introduced a gray cloud deck, the position of which was varied between 100 and 10^{-6} bar, in 1 dex steps. We considered 100 bar to be the cloud-free model, as the atmosphere will become optically thick at lower pressures. The following gas opacities were included: H_2O, CH_4, CO, CO_2, NH_3, PH_3, TiO, VO, Na, K, H_2S, H_2 and He Rayleigh scattering, H2-H2 and H2-He collision-induced absorption. The atmospheric models described above were then retrieved with `petitRADTRANS`, including equilibrium chemistry, using the `PyMultiNest` package (Buchner et al. 2014), which makes use of the nested sampling implementation `MultiNest`, by Feroz et al. (2009). We created synthetic HST observations with the WFC3 instrument, assuming 12 wavelength points spaced equidistantly from 1.12 to 1.65 μm. The error on the flux decrease during transit was assumed to be 33 ppm for TOI-421 b and 35 ppm for TOI-421 c per channel, which we calculated for a single transit of the two planets, using the `Pandexo_HST` tool[13]. For reference, this is about 1/3 of the signal of one atmospheric scale height of TOI-421 b, when assuming a solar composition. For every input model we assumed three different setups of the retrieval model: (i) nominal, using the same model as used to make the observations, (ii) a model neglecting the opacity of CH_4, (iii) a flat line model that only retrieves the planet's radius. The Bayes fac-
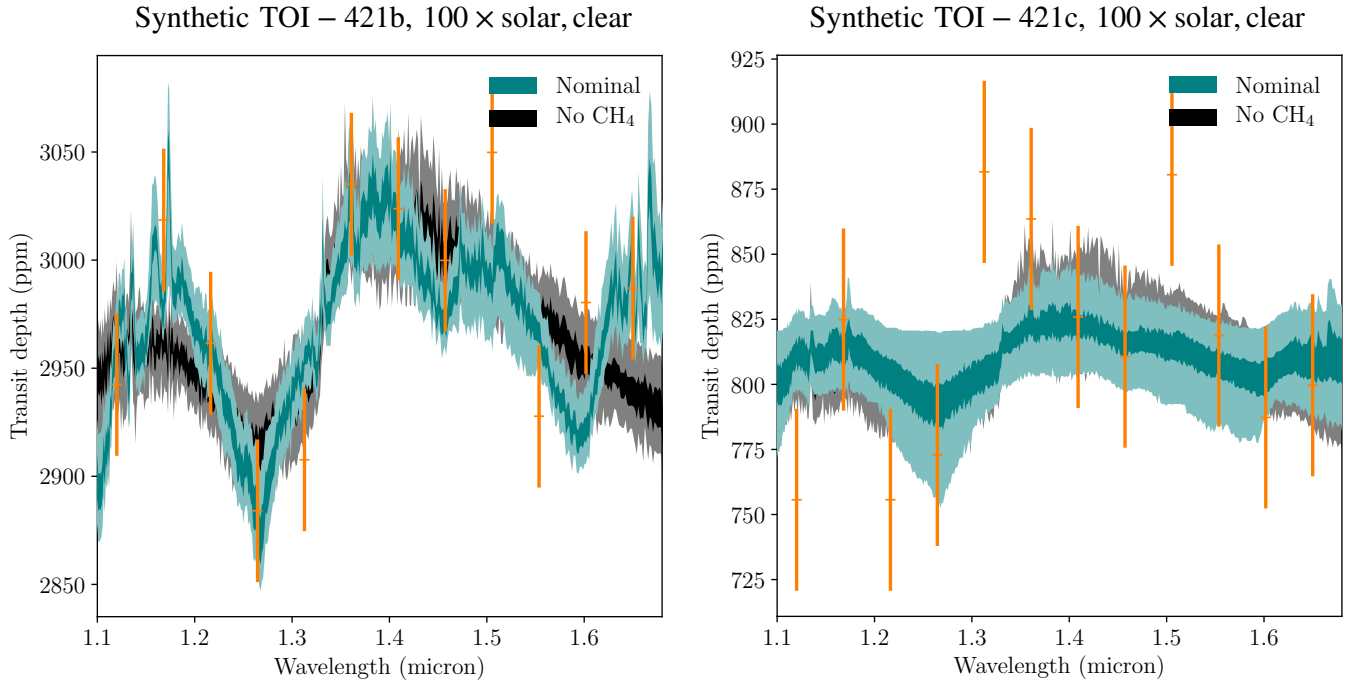
---

[13] https://exoctk.stsci.edu/.

Figure 17. *Left panel:* synthetic HST data of TOI-421 b (orange), and the 1- and 2-σ uncertainty envelopes of the retrievals with the nominal model (blue) and the model that neglected the CH_4 opacity (black). The input data was assuming no clouds and 100 times solar enrichment. *Right panel:* analogous analysis plot for TOI-421 c.

tor B between model (i) and (iii) will constrain how confidently the atmospheric features can be detected, while the B between model (i) and (ii) informs us about how reliably CH_4 can be detected, if the atmosphere is indeed in chemical equilibrium. For models (i) and (ii) the five free parameters were the atmospheric temperature, the reference pressure P_0 at the planet's white light radius, the metallicity [Fe/H] and C/O, as well as the pressure of the gray cloud deck P_{cloud}.

9.3.1. *TOI-421 b*

For the three times solar metallicity case we found that for cloud pressures larger than 0.1 mbar, substantial atmospheric features can be retrieved ($B > 3$, see Kass & Raftery 1995 for a definition of the B thresholds). For a metallicity of 100 times solar, this transition occurs for pressures larger than 0.01 mbar. This value is smaller because the high metallicity atmosphere becomes optically thick at a higher altitude, due to the increased absorption of the more abundant gas molecules. The transition pressure would be even lower if high metallicity atmospheres were not more difficult to observe, because of larger atmospheric mean molecular weights, hence smaller scale heights.

We find that for cloud pressures larger than 1 mbar, the signal of CH_4 can be confidently detected in the atmosphere of the planet, for the 3 times solar enrichment case. For the 100 times solar enrichment case we find a similar transition pressure. In this case, for cloud pressures smaller than 1 mbar, the CH_4 arising from the deeper regions of the atmosphere is cut off by the cloud.

As an example, the left panel of Figure 17 shows the retrievals of the 100 times solar enrichment, clear atmosphere synthetic observation for the model with and without CH_4. In this case the presence of CH_4 in the atmosphere is favored, with a B of 13.

9.3.2. *TOI-421 c*

For the three times solar metallicity case we found that for cloud pressures larger than 1 mbar, substantial atmospheric features can be retrieved. For a metallicity of 100 times solar, this transition occurs for pressures larger than 0.1 mbar. Due to the high equilibrium temperature of the planet, no CH_4 can be detected in the synthetic observations. This is because at high temperatures CO is chemically favored as the main C-bearing species, instead of CH_4.

The right panel of Figure 17 shows the retrievals of the 100 times solar enrichment, clear atmosphere synthetic observation for the model with and without CH_4. In this case there is no difference between the models with or without CH_4.

9.4. *Prospects for detecting transit-timing variation and the Rossiter-McLaughlin effect*

The orbital periods of the two planets are close to a 3:1 commensurability (5.2 and 16.1 days) and therefore transit timing variations (TTVs) are expected. However, given the combined *TESS* and photometric follow-up observation time span of ~80 days, no TTVs have been detected. We investigated possible TTVs through a 3-body simulation using the Python Tool for Transit Variations (PyTTV). We simulated the

estimated TTVs and RVs using the stellar and planetary parameters reported in Table 1 and 3, and found an expected TTV signal with a period of ~180 days and an amplitude of ~4 minutes. However, two issues have prevented a TTV detection. First, the time span from the *TESS* and photometric follow-up observations covers less than half of the expected TTV period, and second the large uncertainties in the individual transit center times of ~1 and 4 minutes for the outer and inner planet, respectively. TOI-421 is an ideal target to compare planetary masses determined from TTVs and RVs in the future with additional transit observations.

Using the RM effect modeling and fitting code described in Esposito et al. (2017), we performed simulations to assess the RV amplitude of the Rossiter-McLaughlin (RM) effect based on our determination of the relevant stellar ($v \sin i_\star$, $R_\star$, limb darkening) and planetary (R_p, b) parameters. We found that for a sky-projected obliquity $\lambda = 0$ deg (90 deg), the amplitude of the RM effect is 2.0 (4.1) m s^{-1} for TOI-421 b. Similarly for TOI-421 c, we found an amplitude of 0.3 (0.9) m s^{-1} for $\lambda = 0$ deg (90 deg). We performed simulations to assess the possibility to measure the RM effect of TOI-421b with HARPS observations. Assuming a time series of spectra with 15 minutes exposure time covering a full transit, and a 2 m s^{-1} error per RV measurement, we estimated that λ could be measured with an uncertainty of $\lesssim 15$ deg.

10. CONCLUSIONS

We presented the discovery of a Neptune-sized planet and a sub-Neptune transiting TOI-421 (BD-14 1137, TIC 94986319), a G9 dwarf star observed by *TESS*. The host star is the primary component of a visual binary. Our RV follow-up observations led to the confirmation of the outer Neptune-sized planet (TOI-421 b) and the discovery of the second inner sub-Neptune (TOI-421 c), that we also found to transit its host star. We determined both stellar and planetary parameters. We found that TOI-421 is a relatively quiet star with an activity index of log R'$_{HK}$ = -4.93 ± 0.04. Based on the analysis of the HARPS and WASP-South data, we found that the intrinsic activity of TOI-421 can be explained mainly by plages.

Our TTV analysis shows that TOI-421 is an ideal target to compare planetary masses determined via TTV and Doppler techniques. We aim for future additional transit observations to explore this in more detail.

TOI-421 b and c are very appealing and suitable targets for atmospheric characterization. They are both expected to host extended atmospheres, showing significant signal in the Ly-α line. Moreover, the atmospheric retrievals demonstrated that we can detect CH$_4$ in the atmosphere of the outer planet (TOI-421 b) if the atmosphere is in chemical equilibrium, and atmospheric evolution simulations showed that the inner planet (TOI-421 c) appears to be among the small sam-
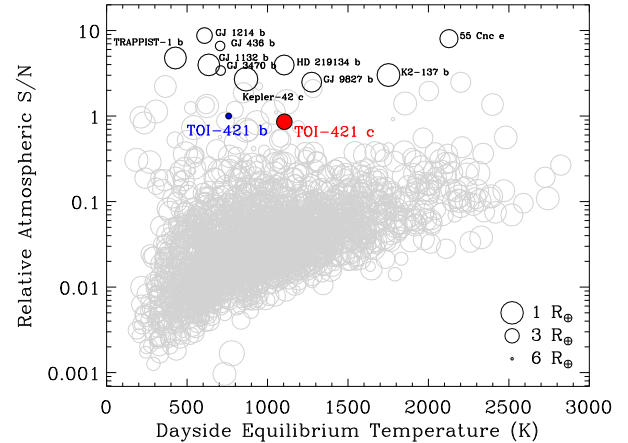

Figure 18. Predicted relative S/N of an atmospheric signal in the *J*-band for all exoplanet candidates with $R < 6 R_\oplus$. The TOI-421 planets are the filled colored symbols with TOI-421b used as the S/N reference. The top ten targets using this metric are labeled. The TOI-421 planets rank in the top 30 most favorable for atmospheric characterization from among more than 2000 exoplanets in this size range.

ple of peculiar super puffy mini-Neptunes, making it also more intriguing for atmospheric studies and evolution theories. This multi-planet system with its astonishing characteristics would be a prime target for the upcoming *JWST* observations. Indeed, the two planets are among the first 30 targets with the highest expected signal-to-noise ratios, as shown in Figure 18. Using the sample of exoplanets with $R < 6 R_\oplus$, totaling more than 2000 exoplanets[14], TOI-421 b and c are within the top 30 most favorable targets for atmospheric characterization. This atmospheric characterization metric is based on a *J*-band, *JWST* style observation, and is detailed in Niraula et al. (2017). Of particular note is this metric is scaled by the frequency of transits. This is motivated by the expectation that sensitive atmospheric observations will likely require many transits to build sufficient signal, and it may be prohibitive to accumulated the needed transits for longer period exoplanets. Therefore, we used a metric that optimizes the S/N over a period of time rather than a per-transit metric. Irregardless of the nuances of the metric, the TOI-421's planets are highly attractive targets for characterization of both their bound and extended atmospheres.

[14] https://exoplanetarchive.ipac.caltech.edu.

Table 4. HARPS RV measurements of TOI-421. (a) Barycentric Julian dates are given in barycentric dynamical time; (b) S/N ratio per pixel at 550 nm.

BJD$^{a}_{TDB}$ -2450000	RV ($km\,s^{-1}$)	σ_{RV} ($km\,s^{-1}$)	BIS ($km\,s^{-1}$)	FWHM ($km\,s^{-1}$)	$\log R'_{HK}$	$\sigma \log R'_{HK}$	T_{exp} (s)	S/N [b]
8528.596454	79.5473	0.0011	-0.0181	6.7449	-4.948	0.019	1200	69
8529.643890	79.5417	0.0013	-0.0198	6.7420	-4.842	0.018	1200	61
8530.589677	79.5415	0.0011	-0.0257	6.7420	-4.978	0.019	1200	73
...								

Table 5. HIRES RV measurements of TOI-421. (a) Barycentric Julian dates are given in barycentric dynamical time; (b) S/N ratio per pixel at 550 nm.

BJD$^{a}_{TDB}$ -2450000	RV ($km\,s^{-1}$)	σ ($km\,s^{-1}$)	T_{exp} (s)	S/N [b]
8744.056124	-0.0047	0.0011	770	218
8777.027485	0.0047	0.0011	592	218
8788.071425	0.0061	0.0011	680	221
...				

Table 6. FIES RV measurements of TOI-421. (a) Barycentric Julian dates are given in barycentric dynamical time; (b) S/N ratio per pixel at 550 nm.

BJD$^{a}_{TDB}$ -2450000	RV ($km\,s^{-1}$)	σ ($km\,s^{-1}$)	T_{exp} (s)	S/N [b]
8517.532619	0.0000	0.0064	1800	65
8522.486513	-0.0070	0.0042	2400	88
8523.431757	-0.0078	0.0046	2400	84
...				

Table 7. PFS RV measurements of TOI-421. (a) Barycentric Julian dates are given in barycentric dynamical time; (b) S/N ratio per pixel at 550 nm.

BJD$^{a}_{TDB}$ -2450000	RV ($km\,s^{-1}$)	σ ($km\,s^{-1}$)	T_{exp} (s)	S/N [b]
8592.508995	-0.0006	0.0009	2400	73
8708.926166	0.0059	0.0009	1200	61
8717.901009	-0.0017	0.0010	1200	50
...				

REFERENCES

Allan, A., & Vidotto, A. A. 2019, MNRAS, 490, 3760

Allard, F., Homeier, D., & Freytag, B. 2012, Philosophical Transactions of the Royal Society of London Series A, 370, 2765

Baranne, A., Queloz, D., Mayor, M., et al. 1996, A&AS, 119, 373

Barclay, T., Pepper, J., & Quintana, E. V. 2018, ApJS, 239, 2

Barragán, O., Gandolfi, D., & Antoniciello, G. 2019, MNRAS, 482, 1017

Barragán, O., Gandolfi, D., Dai, F., et al. 2018, A&A, 612, A95

Bourrier, V., Lecavelier des Etangs, A., Ehrenreich, D., et al. 2018, A&A, 620, A147

Brahm, R., Espinoza, N., Jordán, A., et al. 2019a, AJ, 158, 45

—. 2019b, AJ, 158, 45

Bressan, A., Marigo, P., Girardi, L., et al. 2012, MNRAS, 427, 127

Brown, T. M., Baliber, N., Bianco, F. B., et al. 2013, Publications of the Astronomical Society of the Pacific, 125, 1031

Bruntt, H., Bedding, T. R., Quirion, P.-O., et al. 2010, MNRAS, 405, 1907

Buchhave, L. A., Bakos, G. Á., Hartman, J. D., et al. 2010, ApJ, 720, 1118

Buchner, J., Georgakakis, A., Nandra, K., et al. 2014, A&A, 564, A125

Burnham, K. P., & Anderson, D. R. 2004, Sociological Methods & Research, 33, 261

Butler, R. P., Marcy, G. W., Williams, E., et al. 1996, PASP, 108, 500

Cabrera, J., Csizmadia, S., Erikson, A., Rauer, H., & Kirste, S. 2012, A&A, 548, A44

Cardelli, J. A., Clayton, G. C., & Mathis, J. S. 1989, ApJ, 345, 245

Carleo, I., Malavolta, L., Lanza, A. F., et al. 2020, arXiv e-prints, arXiv:2002.10562

Ceillier, T., Tayar, J., Mathur, S., et al. 2017, A&A, 605, A111

Choi, J., Dotter, A., Conroy, C., et al. 2016, ApJ, 823, 102

Ciardi, D. R., Beichman, C. A., Horch, E. P., & Howell, S. B. 2015, ApJ, 805, 16

Claret, A., & Bloemen, S. 2011, A&A, 529, A75

Collins, K. A., Kielkopf, J. F., Stassun, K. G., & Hessman, F. V. 2017, AJ, 153, 77

Crane, J. D., Shectman, S. A., & Butler, R. P. 2006, Society of Photo-Optical Instrumentation Engineers (SPIE) Conference Series, Vol. 6269, The Carnegie Planet Finder Spectrograph, 626931

Crane, J. D., Shectman, S. A., Butler, R. P., et al. 2010, Society of Photo-Optical Instrumentation Engineers (SPIE) Conference Series, Vol. 7735, The Carnegie Planet Finder Spectrograph: integration and commissioning, 773553

Crane, J. D., Shectman, S. A., Butler, R. P., Thompson, I. B., & Burley, G. S. 2008, Society of Photo-Optical Instrumentation Engineers (SPIE) Conference Series, Vol. 7014, The Carnegie Planet Finder Spectrograph: a status report, 701479

Cubillos, P., Harrington, J., Loredo, T. J., et al. 2017a, AJ, 153, 3

Cubillos, P., Erkaev, N. V., Juvan, I., et al. 2017b, MNRAS, 466, 1868

da Silva, L., Girardi, L., Pasquini, L., et al. 2006, A&A, 458, 609

Dai, F., Winn, J. N., Gandolfi, D., et al. 2017, AJ, 154, 226

Díaz, M. R., Jenkins, J. S., Gand olfi, D., et al. 2020, MNRAS, arXiv:1911.02012

Donati, J. F., & Landstreet, J. D. 2009, ARA&A, 47, 333

dos Santos, L. A., Ehrenreich, D., Bourrier, V., et al. 2020, A&A, 634, L4

Doyle, A. P., Davies, G. R., Smalley, B., Chaplin, W. J., & Elsworth, Y. 2014, MNRAS, 444, 3592

Dragomir, D., Teske, J., Günther, M. N., et al. 2019, ApJL, 875, L7

Dumusque, X., Boisse, I., & Santos, N. C. 2014, ApJ, 796, 132

Esposito, M., Covino, E., Desidera, S., et al. 2017, A&A, 601, A53

Esposito, M., Armstrong, D. J., Gandolfi, D., et al. 2019, A&A, 623, A165

Feroz, F., Hobson, M. P., & Bridges, M. 2009, MNRAS, 398, 1601

Feroz, F., Hobson, M. P., Cameron, E., & Pettitt, A. N. 2013, ArXiv e-prints, arXiv:1306.2144

Fossati, L., Erkaev, N. V., Lammer, H., et al. 2017a, A&A, 598, A90

Fossati, L., Marcelja, S. E., Staab, D., et al. 2017b, A&A, 601, A104

Frandsen, S., & Lindberg, B. 1999, in Astrophysics with the NOT, ed. H. Karttunen & V. Piirola, 71

Fridlund, M., Gaidos, E., Barragán, O., et al. 2017, A&A, 604, A16

Fulton, B. J., Petigura, E. A., Blunt, S., & Sinukoff, E. 2018, PASP, 130, 044504

Furlan, E., Ciardi, D. R., Everett, M. E., et al. 2017, AJ, 153, 71

Gaia Collaboration, Prusti, T., de Bruijne, J. H. J., et al. 2016, A&A, 595, A1

Gaia Collaboration, Brown, A. G. A., Vallenari, A., et al. 2018a, A&A, 616, A1

—. 2018b, A&A, 616, A1

Gandolfi, D., Alcalá, J. M., Leccia, S., et al. 2008, ApJ, 687, 1303

Gandolfi, D., Parviainen, H., Fridlund, M., et al. 2013, A&A, 557, A74

Gandolfi, D., Barragán, O., Hatzes, A. P., et al. 2017, AJ, 154, 123

Gandolfi, D., Barragán, O., Livingston, J. H., et al. 2018, A&A, 619, L10

Gandolfi, D., Fossati, L., Livingston, J. H., et al. 2019, ApJL, 876, L24

Gao, P., & Zhang, X. 2020, ApJ, 890, 93

García, R. A., & Ballot, J. 2019, Living Reviews in Solar Physics, 16, 4

García, R. A., Hekker, S., Stello, D., et al. 2011, MNRAS, 414, L6

García, R. A., Mathur, S., Pires, S., et al. 2014a, A&A, 568, A10

García, R. A., Ceillier, T., Salabert, D., et al. 2014b, A&A, 572, A34

Gelman, A., & Rubin, D. B. 1992, Statistical Science, 7, 457

Grunblatt, S. K., Howard, A. W., & Haywood, R. D. 2015, ApJ, 808, 127

Grziwa, S., & Pätzold, M. 2016, arXiv e-prints, arXiv:1607.08417

Grziwa, S., Gandolfi, D., Csizmadia, S., et al. 2016, AJ, 152, 132

Günther, M. N., Pozuelos, F. J., Dittmann, J. A., et al. 2019, Nature Astronomy, 3, 1099

Hatzes, A. P. 2016, Astrophysics and Space Science Library, Vol. 428, The Radial Velocity Method for the Detection of Exoplanets, ed. V. Bozza, L. Mancini, & A. Sozzetti, 3

Haywood, R. D., Collier Cameron, A., Queloz, D., et al. 2014, MNRAS, 443, 2517

Henden, A. A., Levine, S., Terrell, D., & Welch, D. L. 2015, in American Astronomical Society Meeting Abstracts, Vol. 225, American Astronomical Society Meeting Abstracts #225, 336.16

Hirano, T., Dai, F., Gandolfi, D., et al. 2018, AJ, 155, 127

Howard, A. W., Johnson, J. A., Marcy, G. W., et al. 2010, ApJ, 721, 1467

Huang, C. X., Shporer, A., Dragomir, D., et al. 2018a, arXiv e-prints, arXiv:1807.11129

Huang, C. X., Burt, J., Vanderburg, A., et al. 2018b, ApJL, 868, L39

Husser, T.-O., Wende-von Berg, S., Dreizler, S., et al. 2013, A&A, 553, A6

Jenkins, J. M., Twicken, J. D., McCauliff, S., et al. 2016, Society of Photo-Optical Instrumentation Engineers (SPIE) Conference Series, Vol. 9913, The TESS science processing operations center, 99133E

Jensen, E. 2013, Tapir: A web interface for transit/eclipse observability, Astrophysics Source Code Library, , , ascl:1306.007

Johnstone, C. P., Güdel, M., Brott, I., & Lüftinger, T. 2015a, A&A, 577, A28

Johnstone, C. P., Güdel, M., Stökl, A., et al. 2015b, ApJL, 815, L12

Jordán, A., Brahm, R., Espinoza, N., et al. 2019, arXiv e-prints, arXiv:1911.05574

Kass, R. E., & Raftery, A. E. 1995, Journal of the American Statistical Association, 90, 773

Kipping, D. M. 2013, MNRAS, 435, 2152

Kite, E. S., Fegley, Bruce, J., Schaefer, L., & Ford, E. B. 2019, ApJL, 887, L33

Korth, J., Csizmadia, S., Gandolfi, D., et al. 2019, MNRAS, 482, 1807

Kovács, G., Zucker, S., & Mazeh, T. 2002, A&A, 391, 369

Kubyshkina, D., Fossati, L., Erkaev, N. V., et al. 2018, A&A, 619, A151

Kubyshkina, D., Cubillos, P. E., Fossati, L., et al. 2019a, ApJ, 879, 26

Kubyshkina, D., Fossati, L., Mustill, A. J., et al. 2019b, A&A, 632, A65

Kurucz, R. L. 2013, ATLAS12: Opacity sampling model atmosphere program, Astrophysics Source Code Library, , , ascl:1303.024

Lammer, H., Erkaev, N. V., Fossati, L., et al. 2016, MNRAS, 461, L62

Latham, D. W., Rowe, J. F., Quinn, S. N., et al. 2011, ApJL, 732, L24

Lendl, M., Bouchy, F., Gill, S., et al. 2020, MNRAS, 492, 1761

Libby-Roberts, J. E., Berta-Thompson, Z. K., Désert, J.-M., et al. 2020, AJ, 159, 57

Linsky, J. L., Fontenla, J., & France, K. 2014, ApJ, 780, 61

Linsky, J. L., France, K., & Ayres, T. 2013, ApJ, 766, 69

Lissauer, J. J., Ragozzine, D., Fabrycky, D. C., et al. 2011, ApJS, 197, 8

Lissauer, J. J., Marcy, G. W., Bryson, S. T., et al. 2014, ApJ, 784, 44

Lovis, C., & Pepe, F. 2007, A&A, 468, 1115

Lovis, C., Pepe, F., Bouchy, F., et al. 2006, Society of Photo-Optical Instrumentation Engineers (SPIE) Conference Series, Vol. 6269, The exoplanet hunter HARPS: unequalled accuracy and perspectives toward 1 cm s $^{-1}$ precision, 62690P

Luri, X., Brown, A. G. A., Sarro, L. M., et al. 2018, A&A, 616, A9

Mamajek, E. E., & Hillenbrand, L. A. 2008, ApJ, 687, 1264

Mandel, K., & Agol, E. 2002, ApJL, 580, L171

Mathur, S., García, R. A., Régulo, C., et al. 2010, A&A, 511, A46

Mathur, S., García, R. A., Ballot, J., et al. 2014, A&A, 562, A124

Maxted, P. F. L., Anderson, D. R., Collier Cameron, A., et al. 2011, PASP, 123, 547

Mayor, M., Pepe, F., Queloz, D., et al. 2003, The Messenger, 114, 20

McCully, C., Volgenau, N. H., Harbeck, D.-R., et al. 2018, in Society of Photo-Optical Instrumentation Engineers (SPIE) Conference Series, Vol. 10707, Proc. SPIE, 107070K

Meunier, N., Desort, M., & Lagrange, A.-M. 2010, A&A, 512, A39

Milbourne, T. W., Haywood, R. D., Phillips, D. F., et al. 2019, ApJ, 874, 107

Mollière, P., van Boekel, R., Bouwman, J., et al. 2017, A&A, 600, A10

Mollière, P., Wardenier, J. P., van Boekel, R., et al. 2019, A&A, 627, A67

Morgenthaler, A., Petit, P., Saar, S., et al. 2012, A&A, 540, A138

Morris, R. L., Twicken, J. D., Smith, J. C., et al. 2017, Kepler Data Processing Handbook: Photometric Analysis, Kepler Science Document, ,

Morton, T. D. 2015, isochrones: Stellar model grid package, Astrophysics Source Code Library, , , ascl:1503.010

Murdoch, K. A., Hearnshaw, J. B., & Clark, M. 1993, ApJ, 413, 349

Murray-Clay, R. A., Chiang, E. I., & Murray, N. 2009, ApJ, 693, 23

Niraula, P., Redfield, S., Dai, F., et al. 2017, AJ, 154, 266

Nowak, G., Palle, E., Gandolfi, D., et al. 2017, AJ, 153, 131

Oklopčić, A., & Hirata, C. M. 2018, ApJL, 855, L11

Owen, J. E., & Wu, Y. 2017, ApJ, 847, 29

Parviainen, H., & Aigrain, S. 2015, MNRAS, 453, 3821

Paxton, B., Schwab, J., Bauer, E. B., et al. 2018, ApJS, 234, 34

Pecaut, M. J., & Mamajek, E. E. 2013, ApJS, 208, 9

Pepe, F., Mayor, M., Galland, F., et al. 2002, A&A, 388, 632

Persson, C. M., Fridlund, M., Barragán, O., et al. 2018, A&A, 618, A33

Persson, C. M., Csizmadia, S., Mustill, A. e. J., et al. 2019, A&A, 628, A64

Piskunov, N., & Valenti, J. A. 2017, A&A, 597, A16

Pizzolato, N., Maggio, A., Micela, G., Sciortino, S., & Ventura, P. 2003, A&A, 397, 147

Pollacco, D. L., Skillen, I., Collier Cameron, A., et al. 2006, PASP, 118, 1407

Press, W. H., Teukolsky, S. A., Vetterling, W. T., & Flannery, B. P. 2002, Numerical recipes in C++ : the art of scientific computing

Queloz, D., Mayor, M., Udry, S., et al. 2001, The Messenger, 105, 1

Quinn, S. N., Becker, J. C., Rodriguez, J. E., et al. 2019, AJ, 158, 177

Raghavan, D., McAlister, H. A., Henry, T. J., et al. 2010, ApJS, 190, 1

Ricker, G. R., Winn, J. N., Vanderspek, R., et al. 2014, Society of Photo-Optical Instrumentation Engineers (SPIE) Conference Series, Vol. 9143, Transiting Exoplanet Survey Satellite (TESS), 914320

Rowe, J. F., Bryson, S. T., Marcy, G. W., et al. 2014, ApJ, 784, 45

Ryabchikova, T., Piskunov, N., Kurucz, R. L., et al. 2015, PhyS, 90, 054005

Santos, A. R. G., García, R. A., Mathur, S., et al. 2019, ApJS, 244, 21

Sanz-Forcada, J., Micela, G., Ribas, I., et al. 2011, A&A, 532, A6

Savitzky, A., & Golay, M. J. E. 1964, Analytical Chemistry, 36, 1627

Schofield, M., Chaplin, W. J., Huber, D., et al. 2019, ApJS, 241, 12

Shapiro, A. I., Solanki, S. K., Krivova, N. A., Yeo, K. L., & Schmutz, W. K. 2016, A&A, 589, A46

Skrutskie, M. F., Cutri, R. M., Stiening, R., et al. 2006, AJ, 131, 1163

Smith, J. C., Stumpe, M. C., Van Cleve, J. E., et al. 2012, PASP, 124, 1000

Southworth, J. 2011, MNRAS, 417, 2166

Stassun, K. G., Oelkers, R. J., Pepper, J., et al. 2018, AJ, 156, 102

Stökl, A., Dorfi, E., & Lammer, H. 2015, A&A, 576, A87

Strassmeier, K. G. 2009, A&A Rv, 17, 251

Stumpe, M. C., Smith, J. C., Catanzarite, J. H., et al. 2014, PASP, 126, 100

Stumpe, M. C., Smith, J. C., Van Cleve, J. E., et al. 2012, PASP, 124, 985

Stürmer, J., Seifahrt, A., Schwab, C., et al. 2018, in Society of Photo-Optical Instrumentation Engineers (SPIE) Conference Series, Vol. 10702, Proc. SPIE, 107022S

Sullivan, P. W., Winn, J. N., Berta-Thompson, Z. K., et al. 2015, ApJ, 809, 77

Telting, J. H., Avila, G., Buchhave, L., et al. 2014, Astronomische Nachrichten, 335, 41

Twicken, J. D., Clarke, B. D., Bryson, S. T., et al. 2010, Society of Photo-Optical Instrumentation Engineers (SPIE) Conference Series, Vol. 7740, Photometric analysis in the Kepler Science Operations Center pipeline, 774023

Twicken, J. D., Catanzarite, J. H., Clarke, B. D., et al. 2018, PASP, 130, 064502

Valenti, J. A., & Piskunov, N. 1996, A&AS, 118, 595

Van Eylen, V., & Albrecht, S. 2015, ApJ, 808, 126

Van Eylen, V., Nowak, G., Albrecht, S., et al. 2016, ApJ, 820, 56

Villarreal D'Angelo, C., Esquivel, A., Schneiter, M., & Sgró, M. A. 2018, MNRAS, 479, 3115

Villarreal D'Angelo, C., Schneiter, M., Costa, A., et al. 2014, MNRAS, 438, 1654

Vogt, S. S., Allen, S. L., Bigelow, B. C., et al. 1994, Society of Photo-Optical Instrumentation Engineers (SPIE) Conference Series, Vol. 2198, HIRES: the high-resolution echelle spectrometer on the Keck 10-m Telescope, ed. D. L. Crawford & E. R. Craine, 362

Winn, J. N. 2010, arXiv e-prints, arXiv:1001.2010

Wood, B. E., Redfield, S., Linsky, J. L., Müller, H.-R., & Zank, G. P. 2005, ApJS, 159, 118

Wright, N. J., Drake, J. J., Mamajek, E. E., & Henry, G. W. 2011, ApJ, 743, 48

Yee, S. W., Petigura, E. A., & von Braun, K. 2017, ApJ, 836, 77

Zechmeister, M., & Kürster, M. 2009, A&A, 496, 577

Zeng, L., Sasselov, D. D., & Jacobsen, S. B. 2016, ApJ, 819, 127